CNWRA *A center of excellence in earth sciences and engineering*

A Division of Southwest Research Institute™
6220 Culebra Road • San Antonio, Texas, U.S.A. 78228-5166
(210) 522-5160 • Fax (210) 522-5155

September 6, 2000

U.S. Nuclear Regulatory Commission
ATTN: Mrs. Deborah A. DeMarco
Office of Nuclear Materials Safety and Safeguards
Program Management, Policy Development, and Staff
Office of the Director
Mail Stop 8D-37
Washington, DC 20555

Subject: Transmittal of Journal Paper

Dear Mrs. DeMarco:

The purpose of this letter is to provide you a copy of a paper that will be submitted for publication in Nuclear Instruments & Methods in Physics Research, Section A. The research described in the attached paper, which is entitled, "An Improved *In Situ* Method for Determining Depth Distributions of Gamma-Ray Emitting Radionuclides" is derived from the Ph.D. work of Dr. Roland R. Benke. Because this work was not funded by the NRC you do not need to respond to this letter. However, if you have any questions regarding the content of the paper please contact me at (210) 522-5252 or Dr. Benke at (210) 522-5250.

Sincerely,

Budhi Sagar
Technical Director

GWW/cw
enlcosures

cc:	J. Linehan	K. Stablein	T. McCartin	W. Patrick	T. Nagy (SwRI Contracts)
	B. Meehan	S. Wastler	R. Codell	CNWRA Dirs	P. Maldonado
	E. Whitt	J. Firth	D. Esh	CNWRA EMs	
	J. Greeves		M. Rahimi	R. Benke	
	J. Holonich		B. Eid	J. Weldy	
	W. Reamer		C. McKenney	P. LaPlante	
	T. Essig			M. Smith	

d:\wpfil\gordon\letters\demarco letter 9-6-00.wpd

Washington Office • Twinbrook Metro Plaza #210
12300 Twinbrook Parkway • Rockville, Maryland 20852-1606

AN IMPROVED *IN SITU* METHOD FOR DETERMINING DEPTH DISTRIBUTIONS OF GAMMA-RAY EMITTING RADIONUCLIDES

Roland R. Benke*[†] and Kimberlee J. Kearfott[†]

* now at the Center for Nuclear Waste Regulatory Analyses, Southwest Research Institute, 6220 Culebra Road, San Antonio, TX, 78238-5166, USA

[†] University of Michigan, Department of Nuclear Engineering and Radiological Sciences, 2355 Bonisteel Boulevard, Ann Arbor, MI 48109-2104, USA

Abstract

In situ gamma-ray spectrometry determines the quantities of radionuclides in some medium with a portable detector. The main limitation of *in situ* gamma-ray spectrometry lies in determining the depth distribution of radionuclides. This limitation is addressed by developing an improved *in situ* method for determining the depth distributions of gamma-ray emitting radionuclides in large area sources. This paper implements a unique collimator design with conventional radiation detection equipment. Cylindrically symmetric collimators were fabricated to allow only those gamma-rays emitted from a selected range of polar angles (measured off the detector axis) to be detected. Positioned with its axis normal to surface of the media, each collimator enables the detection of gamma-rays emitted from a different range of polar angles and preferential depths. Previous *in situ* methods require *a priori* knowledge of the depth distribution shape. However, the absolute method presented in this paper determines the depth distribution as a histogram and does not rely on such assumptions. Other advantages over

previous *in situ* methods are that this method only requires a single gamma-ray emission, provides more detailed depth information, and offers a superior ability for characterizing complex depth distributions. Collimated spectrometer measurements of buried area sources demonstrated the capability of the method to yield accurate depth information. Based on the results of actual measurements, this method increases the potential of *in situ* gamma-ray spectrometry as an independent characterization tool in situations with unknown radionuclide depth distributions.

Keywords: Depth distribution; radionuclide characterization; *in situ*; gamma-ray spectrometry; nondestructive evaluation; collimation.

Introduction

In principle, *in situ* gamma-ray spectrometry uses a portable detector to quantify the amount of radionuclides in some medium. In comparison, the more established method of laboratory gamma-ray spectroscopy consists of taking small samples of the medium into the laboratory for gamma-ray analysis. *In situ* gamma-ray spectrometry characterizes a larger volume of material, requires less time to determine accurate radionuclide concentrations, and minimizes worker doses and the risk of radioactive contamination. The main limitation of *in situ* gamma-ray spectrometry lies in determining the depth distribution of radionuclides [1,2,3]. Therefore, an *in situ* method was developed to address this limitation.

In general, radionuclide depth distributions aid conventional *in situ* gamma-ray spectrometry in determining accurate radionuclide inventories and surface dose rates from individual radionuclides. Depth distributions also represent reliable data for radionuclide

transport studies. Indications of neutron or energetic charged particle fluxes can result from determinations of the activation as a function of material depth. For decontamination and decommissioning activities, the radionuclide depth distribution determines the amount of material that must be remediated to satisfy the release limits.

Three *in situ* gamma-ray spectroscopic methods have been used to determine the depth distribution of radionuclides in soil. These three *in situ* methods are based on multiple photopeak responses, the photopeak-to-valley ratio, and the attenuation of a lead plate. Each method requires *a priori* assumptions of the depth distribution function and uses a gamma-ray spectrometer. Spectrometers allow the users to decipher the energies of gamma-ray emissions, a necessity for determining the specific radioisotope present. In addition to usually assuming a uniform soil density with depth, all three approaches for determining depth distributions also assume a spatially uniform radionuclide distribution.

In a comparison of the three methods, MacDonald et al. [4] calculated ^{137}Cs inventories (with units of Bq m^{-2}, resulting from the integration of the activity concentrations over depth) over a range of depth distributions and found that the lead plate method resulted in the lowest inventory uncertainties. Table 1 summarizes the advantages and disadvantages of the three *in situ* methods.

In addition to the three *in situ* methods for determining depth distributions, spectroscopic measurements in boreholes have also been studied for applications in oil wells [5,6,7]. Because boring itself qualifies as an invasive process, borehole measurements should be considered as quasi-*in-situ* approach. In addition to increased contamination risks, borehole measurements require boring equipment and custom fabricated detection equipment (extended cryostat lengths for HPGe detectors).

Multiple Photopeak Method

For *in situ* gamma-ray measurements of radionuclides in soil, the detector's photopeak count rate is dependent on the radionuclide inventory (activity per unit area of soil), depth distribution, gamma-ray yield, gamma-ray detection efficiency, and attenuation of soil. The gamma-ray yields for radioactive decay are well known quantities. The detection efficiency and soil attenuation coefficient are dependent on the gamma-ray energy and can be measured in the laboratory. Because the multiple photopeak method is based on the detection of two gamma-ray emissions from the same radionuclide, the same radionuclide inventory and depth distribution will apply to each of its gamma-ray emissions. Once the gamma-ray yields, detection efficiencies, and soil attenuation coefficients of each gamma-ray emission are accounted for, the two unknowns (radionuclide inventory and depth distribution) can be determined from two measurements: photopeak count rates corresponding to each gamma-ray emission.

The multiple photopeak method requires *a priori* knowledge of the depth distribution and cannot yield any depth distribution information for radionuclides that emit fewer than two significant gamma-ray energies. Based on the energy-dependence of gamma-ray attenuation, Korun et al. [8] and Rybacek and Jacob [9] applied the multiple photopeak method to ^{134}Cs and ^{137}Cs contamination in soil. Other variations of the multiple photopeak method have also been presented [2,10]. Naessens and Xu [11] incorporated point kernel techniques into a multiple photopeak method to determine the depth information of radionuclides using *in situ* gamma-ray spectrometry. Their method also required *a priori* knowledge of the radionuclide distribution and required the analysis of at least two gamma-ray emissions.

Photopeak-to-Valley Method

Zombori et al. [12] realized that the single forward-scattering gamma-ray detection rate was dependent on the source depth distribution in an attenuating medium. They developed a method based on the ratio of count rates between the 662 keV photopeak and 631-649 keV valley region, between the Compton edge and ^{137}Cs photopeak. As a gamma-ray source moves deeper into an attenuating medium, the photopeak count rate decreases and the valley count rate increases. Therefore, the ratio of the photopeak count rate to the count rate in the valley region (photopeak-to-valley ratio) decreases. This photopeak-to-valley method is applicable to single gamma-ray emitters. However, the method's feasibility is dependent on the intensity of gamma-ray emissions. It can be therefore adversely affected by interfering gamma-ray emissions at energies close to the photopeak or valley region.

To improve the *in situ* activity estimates for ^{137}Cs distributed in a Scottish salt marsh, Tyler et al. [13] used the photopeak-to-valley method on measurements from a cylindrical NaI(Tl) detector with a length of 7.6 cm and diameter of 7.6 cm to estimate a single depth parameter, the mean relaxation mass per unit area. Because the photopeak-to-valley method only yields information about a single depth parameter, the technique can only be effectively applied to simple profile shapes. Using the photopeak-to-valley method with a HPGe detector in the same Scottish salt marsh, Tyler [14] discovered only a marginal improvement in the precision of the *in situ* results over the results from a NaI(Tl) detector. Tyler [14] also concluded that the accuracy of the *in situ* determinations was limited by variations in the shape of the radionuclide depth distribution. No direct comparisons were made of the *in situ* or laboratory determinations of the ^{137}Cs specific activities at different depths.

Chesnokov et al. [15] also made use of the ratio of unscattered and scattered detector responses with a fixed-angle, downward-facing collimator. Similar to the photopeak-to-valley method, the collimated spectrum sensitive (CSSD) method also required assumptions of the depth distribution shape and determined a single depth parameter. Golosov et al. [16] also employed a portable NaI(Tl) scintillation detector with the CSSD technique and assumed a depth distribution of ^{137}Cs that was typical for the specific region. In the high-contamination areas investigated, Golosov et al. [16] concluded that the *in situ* determinations of ^{137}Cs inventories agreed sufficiently well with the collected soil sample results and, therefore, could used an alternative to field sampling. Golosov et al. [16] also mentioned that a HPGe detector might be required to identify lower ^{137}Cs inventories within the gamma-ray background from other radionuclides in soil.

Lead Plate Method

By placing a lead plate in front of an *in situ* detector as depicted in Fig. 1, Korun et al. [17] showed that the response of the detector above the ground is dependent on the distance of the plate from the detector. The uncollided (or unscattered) gamma-rays incident on the detector at large polar angles, measured from the axis of the cylindrical detector crystal, originate predominately from shallower layers of soil. By attenuating the gamma-rays emitted directly beneath the detector with a lead plate, the detector will thus respond primarily to the gamma-rays emitted in the shallower layers of soil. The main advantage of the lead plate method is its applicability to radionuclides, which emit gamma-rays at a single energy. MacDonald et al. [18] performed theoretical assessments of the lead plate method within a borehole for determining radionuclide depth distributions.

Theory

The theoretical derivations of the *in situ* gamma-ray spectrometry calibration factor and gamma-ray fluxes are presented. As applied to the *in situ* measurements of buried area sources, the theoretical relationships for the collimator calibrations, area source activity predictions, and distributed source reconstructions are also included.

Calibration Factor Derivations

The following section introduces the *in situ* gamma-ray spectroscopy calibration factors. Although the following descriptions use soil as the source matrix, other materials (such as concrete or steel) could be substituted as the source matrix. Derivations of the total *in situ* calibration factor have been presented in other studies [19,20,21]:

$$\frac{N_f(E)}{S} = \frac{N_f(E)}{N_0(E)} \cdot \frac{N_0(E)}{\phi(E)} \cdot \frac{\phi(E)}{S} \qquad (1)$$

where $\frac{N_f(E)}{N_0(E)}$ represents the angular correction factor which accounts for the angular nonuniformity of the detector response and incident flux, $\frac{N_0(E)}{\phi(E)}$ is a detector dependent quantity representing the on-axis detector response, and $\frac{\phi(E)}{S}$ is a factor dependent on the source geometry with $\phi(E)$ representing the total uncollided gamma-ray flux incident on the detector at energy E from any angle. S is the generic gamma-ray emission rate and can take two specific forms, S_m or S_A. With units of $\gamma\ s^{-1}\ kg^{-1}$, S_m refers to the gamma-ray emission rate for a uniform distribution and is equal to the gamma-ray emission rate per unit volume divided the density of the material. With units of $\gamma\ s^{-1}\ m^{-2}$, S_A refers to the gamma-ray emission rate for an planar

distribution or an exponential depth distribution where the radionuclide activity is integrated to an infinite depth. The generic gamma-ray emission rate, S, can be converted to radionuclide specific activity (with units of Bq kg^{-1}) by dividing S_m by the gamma-ray yield per decay or converted to radionuclide inventory (with units of Bq m^{-2}) by dividing S_A by the gamma-ray yield per decay

Dropping the f-subscript and energy dependency to simplify the notation of the total *in situ* calibration factor, the radionuclide specific activity in units of Bq kg^{-1} for a uniform radionuclide distribution is calculated from a measured gamma-ray spectrum in the following manner:

$$\text{Specific Activity} = \frac{\text{Photopeak count rate}}{\frac{N}{S_m} \cdot Y} \tag{2}$$

where Y is gamma-ray yield per decay with units of $\gamma\ s^{-1}\ Bq^{-1}$. For a planar or exponential depth distribution, the radionuclide inventory in units of Bq m^{-2} is computed from the following expression:

$$\text{Inventory} = \frac{\text{Photopeak count rate}}{\frac{N}{S_A} \cdot Y}. \tag{3}$$

Gamma-Ray Flux Calculations

Because the measurements presented later in this paper used large area sources, the calculation of the gamma-ray flux was performed for planar source geometry, shown in Fig. 2. To determine the total gamma-ray flux from an infinite plane source buried at a depth, z_{plane}, in soil requires a double integration over the area of the source. Accounting for the gamma-ray attenuation from soil and air, the total gamma-ray flux becomes:

$$\phi_{total}^{plane} = \int_0^{2\pi} \int_0^{\infty} \frac{S_A}{4\pi\rho^2} e^{-\mu_s z_{plane} \sec\theta} e^{-\mu_a h \cdot \sec\theta} r \, dr \, d\varphi \qquad (4)$$

where S_A is the gamma-ray emission rate per unit area with units of $\gamma\ s^{-1}\ cm^{-2}$, ρ is the total distance from the detector to the infinitesimal area of the source with units of cm, μ_s is the soil attenuation coefficient in units of cm^{-1}, μ_a is the air attenuation coefficient in units of cm^{-1}, θ is the off-axis polar angle of the radionuclide measured from the axis of the detector in units of radians, φ is the azimuthal angle in units of radians, and h is the height of the detector above the soil surface in units of cm. The following describes the components of Eq. (4):

$\frac{S_A}{4\pi\rho^2}$ represents the flux a distance ρ from a point source,

$e^{-\mu_s z_{plane} \sec\theta}$ represents the soil attenuation,

$e^{-\mu_a (h \sec\theta)}$ represents the air attenuation, and

$r\ dr\ d\varphi$ represents the Jacobian for a infinitesimal area of the source, dA. Integrating Eq. (4) with respect to the azimuthal angle, substituting $z_{plane} \sec\theta = \rho - \rho_{air}$ and $h \sec\theta = \rho_{air}$, and making a change of variables results in:

$$\phi_{total}^{plane} = \frac{S_A}{2} \int_{h + z_{plane}}^{\infty} \frac{e^{-\mu_s (\rho - \rho_{air}) - \mu_a (\rho_{air})}}{\rho} d\rho \qquad (5)$$

where $\rho^2 = (h + z_{plane})^2 + r^2$ and $\rho\ d\rho = r\ dr$. Using similar triangles, the following relation $\frac{\rho_{air}}{h} = \frac{\rho}{h + z_{plane}}$ proves beneficial. Now putting ρ_{air} in terms of ρ results in:

$$\phi_{total}^{plane} = \frac{S_A}{2} \int_{h + z_{plane}}^{\infty} \frac{e^{-\left(\mu_s \frac{z_{plane}}{h + z_{plane}} + \mu_a \frac{h}{h + z_{plane}}\right)\rho}}{\rho} d\rho \qquad (6)$$

The definition of the exponential integral [22] for n = {0, 1, 2, 3, ...} and for a real x > 0 is:

$$E_n(x) = \int_1^{\infty} \frac{e^{-xt}}{t^n} dt \ , \tag{7}$$

Now to put Eq. (6) in terms of Eq. (7) requires another change of variables:

$$\phi_{total}^{plane} = \frac{S_A}{2} \int_1^{\infty} \frac{e^{-(\mu_s z_{plane} + \mu_a h)t}}{t} \, dt \tag{8}$$

where $t = \rho / (h + z_{plane})$ and $dt / t = d\rho / \rho$. The solution for the total gamma-ray flux from an infinite plane source buried at a soil depth of z_{plane}:

$$\phi_{total}^{plane} = \frac{S_A}{2} E_1\left(\mu_s z_{plane} + \mu_a h\right) \tag{9}$$

Because the collimators limited the detector's field of view, new calculations of the gamma-ray flux were required. The following new derivations of the $\frac{\phi(E)}{S}$ term were used in the experimental calibration of the collimation method. For this limited polar angle case with a planar source, the relationship, $t = \rho/(h + z) = sec\ \theta = \omega$, can be deduced from Fig. 2, and Eq. (8) takes the following form:

$$\phi_{limited}^{plane} = \frac{S_A}{2} \int_{\omega_1}^{\omega_2} \frac{e^{-(\mu_s z_{plane} + \mu_a h)t}}{t} \, dt \tag{10}$$

where $\omega_1 < \omega_2$ (or $\theta_1 < \theta_2$). Solving Eq. (10) by manipulating the limits of integration, the gamma-ray flux for the limited polar angle case from an infinite planar source distribution becomes:

$$\phi_{limited}^{plane} = \frac{S_A}{2}\left[E_1\left(\mu_s z_{plane}\,\omega_1 + \mu_a h\,\omega_1\right) - E_1\left(\mu_s z_{plane}\,\omega_2 + \mu_a h\,\omega_2\right)\right] \tag{11}$$

In the case of a detector responding to multiple planar sources at different depths, the total gamma-ray flux becomes the summation of the individual planar sources, Eq. (11), with the appropriate z_{plane} value for each source. Because the flux from each plane source is calculated

independently, the gamma-ray flux from multiple sources simply becomes the summation of the individual fluxes from each plane source contained in that thickness of soil.

Activity Characterizations of the Area Sources

The creation and characterizations of the ^{134}Cs area sources are presented in the Materials and Methods section. Because the area sources were 102 cm by 102 cm squares and their activities were determined from measurements using a bare detector, rectangular coordinates were used to calculate the gamma-ray flux at the detector. The numerical values for the terms in Eqs. (12) and (13) were used in the activity characterizations. The gamma-ray flux for a unit emission rate per unit source area, ϕ_{bare}/S_A, was calculated from the numerical integration of the following quantity:

$$\frac{\phi_{bare}}{S_A} = \int_0^{y_{max}} \int_0^{x_{max}} \frac{e^{-\mu_{air}\sqrt{x^2+y^2+h^2}}}{\pi\left(x^2+y^2+h^2\right)} dx\ dy \qquad (12)$$

where h represents the height of the detector above the area source (1 m), μ_{air} represents the linear attenuation coefficient for air (0.000091 cm^{-1} for 800 keV gamma-rays in air, [23]), and x_{max} = 50.8 cm and y_{max} = 50.8 cm represent the limits of integration for the square area sources.

Inserting the calibration factor given by Eq. (12) into Eq. (1) and solving for the source emission rate per unit area, S_A in units of $\gamma\ cm^{-2}\ s^{-1}$, results in following relationship (after canceling the N_o terms and dropping the f-subscript and bare-subscript notation):

$$S_A = \frac{N_{meas}}{\left(\frac{N}{\phi}\right)\cdot\left(\frac{\phi}{S_A}\right)} \qquad (13)$$

where N_{meas} represents the measured photopeak count rate with units of min^{-1}, N/ϕ represents the photopeak detector efficiency with units of counts/min per γ cm^{-2} s^{-1}, and ϕ/S_A (unitless) represents gamma-ray flux for a unit gamma-ray emission rate per source area. N/ϕ was measured to be 1328 counts/min per γ cm^{-2} s^{-1} from the 796 and 802 keV summation photopeak of ^{134}Cs with the cylindrical NaI detector with a length of 7.6 cm and diameter of 7.6 cm. To obtain the total activity for a particular area source, the S_A value from Eq. (13) was multiplied by the source area (equal to 10,300 cm^2) and divided by the gamma-ray yield per decay (0.941 γ s^{-1} Bq^{-1} for the 796 and 802 keV gamma-rays of ^{134}Cs).

Collimator Calibrations

In Eq. (13), N/ϕ represents the detector response (photopeak count rate) to a unit gamma-ray flux. N/ϕ can also be interpreted as the detection efficiency for a particular geometry. In order to determine the detection efficiency for each collimator from an area source, experiments were performed with Source A (refer to the Materials and Methods section) placed at different distances. Therefore, the photopeak count rate for a unit gamma-ray emission rate per area at a particular depth, d, in some medium is referred to as the N/S_A calibration factor and computed in the following manner:

$$\frac{N}{S_A}(d) = \frac{N}{\phi}(d) \cdot \frac{\phi}{S_A}(d) \qquad (14)$$

where the N/ϕ values were based on the area source measurements in air and the ϕ/S_A values were calculated to account for the attenuation by the specific materials encountered for a unit source at a particular depth.

Determining the Activity of Multiple Area Sources at Different Depths

The two-source setup refers to two area sources buried beneath different thicknesses of attenuating materials. When two measurements are taken with different collimators, a system of two equations for the measured photopeak count rates arises with two source activity unknowns, a_1 and a_2. Eq. (15) corresponds to the 0-34° collimator measurement, while Eq. (16) corresponds to the 60-70° collimator measurement:

$$R(0-34°) = \frac{Y}{B_{area}} \cdot \left[\frac{N}{S_A}(d_1) \cdot a_1 + \frac{N}{S_A}(d_2) \cdot a_2 \right]. \quad (15)$$

and

$$R(63-72°) = \frac{Y}{B_{area}} \cdot \left[\frac{N}{S_A}(d_1) \cdot a_1 + \frac{N}{S_A}(d_2) \cdot a_2 \right]. \quad (16)$$

where the N/S_A values in units of min^{-1} per γ cm^{-2} s^{-1} are calculated from Eq. (14),

R(0-34°) is the photopeak count rate with the 0-34° collimator in units of min^{-1},

R(60-70°) is the photopeak count rate with the 60-70° collimator in units of min^{-1},

d_1 represents the concrete depth of Source 1,

d_2 represents the concrete depth of Source 2,

a_1 represents the activity of the area source at the depth d_1 in units of Bq,

a_2 represents the activity of the area source at the depth d_2 in units of Bq,

Y represents the gamma-ray yield per decay with units of γ s^{-1} Bq^{-1}, and

B_{area} represents the source surface area (equal to 10,300 cm^2).

In a more general form, the system of equations for multiple sources can be described by:

$$R_i = \sum_{j=1}^{n} \varepsilon_{i,j} \cdot s_j \qquad \text{for } i = 1 \,..\, m \qquad (17)$$

where R_i represents the photopeak count rate measured with the i^{th} collimator,

$\varepsilon_{i,j}$ represents the gamma-ray counting efficiency for the j^{th} source with the i^{th} collimator (ie., the photopeak count rate for a unit gamma-ray emission rate from the source, unitless),

s_j represents the gamma-ray emission rate for the j^{th} source (equal to the source activity multiplied by the gamma-ray yield),

n equals the number of sources, and

m equals the number of collimated measurements.

The counting efficiencies ($\varepsilon_{i,j}$) can be determined experimentally, as N/S_A divided by B_{area}, or computed from Monte Carlo simulations.

For the activity reconstructions, the solutions for the area source activities were determined by minimizing the following quantity:

$$\sum_{i=1}^{m} \sum_{k=1}^{p} \frac{\left(R_{i,k}^{fit} - R_{i,k}^{meas}\right)^2}{R_{i,k}^{meas}} \qquad (18)$$

where $R_{i,k}^{meas}$ represents the measured photopeak count rate, for the k^{th} gamma-ray energy with the i^{th} collimator, p equals the number of gamma-ray energies analyzed, and m equals the number of collimated measurements. $R_{i,k}^{fit}$ represents the fitted photopeak count rate, for the k^{th} gamma-ray energy with the i^{th} collimator and is described by the following relationship:

$$R_{i,k}^{fit} = \sum_{j=1}^{n} \left(\varepsilon_{i,j,k} \cdot Y_k \cdot a_j\right) \qquad (19)$$

where $\varepsilon_{i,j,k}$ represents the gamma-ray counting efficiency (unitless) for the k^{th} gamma-ray energy of the j^{th} source for the i^{th} collimator, Y_k represents the gamma-ray yield per decay (in units of γ s^{-1} Bq^{-1}) for the k^{th} gamma-ray, a_j represents the activity of the j^{th} source in units of Bq, and n equals the number of sources. A non-negativity activity constraint was applied to all of the reconstructions. Without normalizing the square of the count rate difference by the measured count rate, the solution would be skewed to better fit the measurements with the higher count rates, because higher count rates imply larger magnitudes of the count rate differences and much larger squares of the count rate difference.

For the measurements presented in this paper, Eqs. (3-59) and (3-60) were applied to activity reconstructions based on a single gamma-ray emission, implying p = 1. For the analyses based on a single gamma-ray emission, the notation for the k^{th} gamma-ray and the summation over the gamma-ray emissions can be omitted in Eqs. (18) and (19).

Calibration Factor Determinations for the Distributed Source Reconstructions

Experimental determinations of the total *in situ* calibration factor, N/S_A, for the distributed source reconstructions incorporated the area source calibration measurements for each collimator. For each combination of collimator and depth layer, computation of N/S_A for the distributed source reconstructions became the depth-averaged quantity of Eq. (14) over the k^{th} depth layer thickness:

$$\left(\frac{N}{S_A}\right)_k = \frac{\int_{z_{min,k}}^{z_{max,k}} \left[\frac{N}{\phi}(z)\cdot\frac{\phi}{S_A}(z)\right] dz}{\int_{z_{min,k}}^{z_{max,k}} dz} \qquad (20)$$

where the N/ϕ values were based on the area source measurements in air for a specific collimator, the ϕ/S_A values were calculated from Eq. (11) for the specific materials that compose the k^{th} depth layer and those depth layers between the k^{th} depth layer and the surface, $z_{max,k}$ denotes the maximum depth of the k^{th} layer with respect to the surface, and $z_{min,k}$ denotes the minimum depth of the k^{th} layer with respect to the surface.

Collimator Descirption

The method presented in this paper required collimation that limited the detector response to a specific range of polar angles. As shown in Fig. 2, a cylindrical detector was positioned so its axis is normal to the measurement surface. The polar angles were measured off the axis of the cylindrical detector and from the center of the detector crystal. To enable greater counting efficiencies and improved system sensitivity, the collimator design allowed contributions from the entire azimuthal field of view. The azimuthal angle was defined as the angle of rotation about the axis of the detector. By allowing a full azimuthal field of view, larger volumes of source media were characterized with each collimator measurement, thereby offering a more representative result as well as reducing the required counting times.

To accomplish these design criteria, cylindrically symmetric collimators were fabricated using lead. As an example, a cross-sectional view of the collimator design is presented in Fig. 3. Each collimator was designed with sloping edges that matched the desired polar angle. Maximizing the gamma-ray path length through the lead, the sloping edges minimized the contributions from those gamma-rays emitted outside the collimated region of interest.

Because laboratory measurements were planned with 102-cm by 102-cm area sources, the maximum polar angle sampled was limited to 80°. Measurements at polar angles greater

than 80° require much larger experimental geometries. For instance compared to 80°, maximum polar angles of 85° and 88° would require measurement setups over four and twenty-five times larger, respectively, in both area and volume.

The polar angle ranges of the fabricated collimators were 0-34°, 42-60°, 60-70°, and 70-80°. Figs. 4 (a)-(d) display the dimensions of the 0-34°, 42-60°, 60-70°, and 70-80° collimators, respectively. In general as the polar angle is increased, the detector response to uncollided gamma-rays (i.e., photopeak count rate) becomes more dependent on the radionuclide concentration near the source surface [25]. Therefore, large polar angle measurements characterize radionuclide activities in upper layers of soil. Subtracting the upper layers' contributions, the smaller polar angle measurements can be used to determine radionuclide activities in the lower soil layers. The radionuclide activities in each layer are independent and could be used to identify appropriate depth distribution functions, if such a refinement is deemed advantageous.

Calibration Measurements

To test the ability of the collimation method to determine depth information, area sources were created and placed at various depths in attenuating materials. Throughout this paper, a 2048-channel gamma-ray spectroscopy system[1] with a cylindrical NaI(Tl) detector (length of 7.6 cm and diameter of 7.6 cm) was used with the lead collimators depicted in Fig. 4. In addition to point source calibrations, this section discusses the creation of large area sources as well as determinations of the activity and uniformity of those area sources. Experimental calibration measurements of the collimators using the area sources are also presented. Background subtraction was included for all measurements of the net photopeak count rates.

Point Source Measurements

A single ^{134}Cs point source, with an activity of 525 kBq (14.2 μCi) on 4/24/99, was used for all of the point source measurements described below. For each attenuating material used, attenuation measurements were performed by acquiring photopeak count rate data for the point source positioned on-axis behind different material thicknesses. The linear attenuation coefficients for the 796 + 802 keV gamma-rays were determined to be 0.15 cm^{-1} for concrete, 0.19 cm^{-1} for aluminum, and 0.03 cm^{-1} for wood. When compared to other published values, the determined attenuation coefficients are within 1.6% for concrete and 2% for aluminum [24,23]. The attenuation coefficients are used in the computation of the ϕ/S_A term in Eq. (14) for the actual measurement setups where the area sources are buried beneath layers of concrete, aluminum, and wood.

Area Source Creation and Activity Characterizations

Area sources were created by spreading paint, spiked with ^{134}Cs, over 102 cm by 102 cm plywood boards (Lauan was the brand of sandwiched plywood where Mahogany is the species of wood). The plywood boards were coated with an oil-based primer and allowed to dry. A liquid solution of ^{134}Cs, containing the desired ^{134}Cs activity, was added to approximately 100 mL of water-based paint in a plastic beaker. It is important to note that not all of the ^{134}Cs activity added to the paint will be transferred to the area source, some will remain in the paint residue on the paintbrushes, stirring stick, and in the plastic beaker. The objective was to create reasonably uniform area sources with significantly different activities of ^{134}Cs that differ by at least a factor

of three (not to establish a procedure to create an area source for a particular activity within some small tolerance).

Sources with significantly different activities were desirable to test if the presented method would assign the correct activities to each area source from collimated measurements of all three sources buried at different depths. To assess the capability of the collimation method to yield accurate depth information, the area source activities were compared to those predicted by the collimation method for the measurement setups. Since the area source activities were determined from actual measurements instead of estimated from the creation process, precise activity determinations of the paint residue were not required to infer the ^{134}Cs activity on the area sources. The area source activities were decay corrected for all comparisons.

The spiked paint was stirred by hand for at least 3 min and applied on the plywood boards in several coats using paintbrushes. When the amount of paint remaining was less than that required for another full coat, a majority of the remaining paint was applied to the specific locations, determined from visual inspection, with noticeably thinner coats of paint. After the paint dried, the individual boards were wrapped in polyethylene sheeting with a thickness of 0.1 mm. To facilitate easier disposal, each 102 cm by 102 cm area source consisted of six smaller sections: two 61.0 cm by 40.6 cm boards, two 40.6 cm by 40.6 cm boards, one 61.0 cm by 20.3 cm board, and one 40.6 cm by 20.3 cm board.

With a half-life of 2.062 y, the significant gamma-ray emissions for ^{134}Cs are presented in Table 2. Due to the poor energy resolution of the NaI(Tl) detector, the photopeaks from the 796 and 802 keV gamma-ray emissions overlap with one another and could not be resolved separately (the same was true for the 563, 569, and 605 keV emissions). In addition, the gamma-ray emissions of 563, 569, and 605 keV encountered interference with radon and thoron progeny

in the laboratory background. To overcome the radon and thoron interference, all gamma-ray spectroscopic analyses for ^{134}Cs determined the count rate of summation photopeak for the 796 and 802 keV gamma-ray emissions (referred to as 796 + 802 keV for notational convenience).

The area source activities were measured by positioning the NaI(Tl) detector at 1 m above the center of the area source. Performing the numerical integration in Eq. (12) yielded an uncollided gamma-ray flux for a unit gamma-ray emission rate per source area, ϕ/S_A, of 0.073 (unitless), which represents the flux (with units of $\gamma\ cm^{-2}\ s^{-1}$) of 796 + 802 keV gamma-rays incident on the detector for a gamma-ray emission rate of 1 $\gamma\ cm^{-2}\ s^{-1}$ (ie., one gamma-ray emitted per second from each square centimeter of the area source). Using the photopeak count rate measurement for each area source, the gamma-ray emission rates per unit area, S_A, for each source were calculated from Eq. (13). The gamma-ray emission rates per unit area were then converted into total activities for each source. Throughout this paper, the three area sources are referred to as Sources A, B, and C, and their activities are presented in Table 3. The 2σ uncertainties presented in Table 3 were estimated from uncertainties in the measured photopeak count rates due to counting statistics, the angular response of the detector, geometrical representation of the area source as a perfectly flat square, and nonuniformities in the area source activity. The uncertainty associated with the angular response of the detector was estimated at 3%. The uncertainty induced by geometrical representations of the actual area source for the gamma-ray flux calculations was conservatively estimated at 2.5%. To assess the area source nonuniformity, lead bricks were positioned around the bare NaI(Tl) detector to focus the detector response on a small portion of each area source. Using this focussed geometry, measurements were performed over each area source to determine the degree of nonuniformity. Ultimately, the

area source nonuniformity was accounted for by including an estimated 5% uncertainty in the activity for Source A and 10% uncertainty in the activities for Sources B and C.

Area Source Calibrations for each Collimator

In this section, the reader may find it helpful to refer to the Theory section for definitions and relationships of the *in situ* calibration factors. For several source distances in air, the N/ϕ calibration factors (ie., gamma-ray detection efficiencies) for each collimator were determined from photopeak count rate measurements of Source A and calculations of the uncollided gamma-ray flux using Eq. (11). Background measurements of the lead used to fabricate the collimators did not identify radioactive contamination, which would adversely affect the calibration and validation measurements. The values and curve fits of the N/ϕ calibration factor as function of distance in air are presented in Fig. 5(a)-(d) for the 0-34°, 42-60°, 60-70°, and 70-80° collimators, respectively. For the 70-80° collimator measurements of the area sources beneath absorber materials, the ϕ/S_A calibration factor decreases sharply for increasing depths. Therefore, measurements of the N/ϕ calibration factor with the 70-80° collimator were only required for depths between 0-12 cm.

After the calibrations in air were complete, collimated measurements were acquired from burying the area sources at different depths in attenuating materials. The *in situ* calibration factors were determined for each area source location. The N/ϕ value was determined from the fitted curve for the appropriate collimator and source depth. The ϕ/S_A calibration factor for an area source at a depth z below the surface was calculated from Eq. (11) using the polar angle range for the specific collimator employed and the measured linear attenuation coefficients of the materials involved. Because the source distributions are planar, the total *in situ* calibration factor

takes the notational form of N/S_A. The N/S_A values for each collimator and source location were then calculated from Eq. (14).

For the area source measurements, two collimator locations were chosen. Measurements using the 0-34° collimator were taken at the center of the area sources and referred to as the full geometry shown in Fig. 6. The field of view of the collimators with larger values of the polar angle exceeded the dimension of the area sources in the full geometry. Therefore, all measurements (except for the 0-34° collimator measurements) of the buried area sources were taken normal to the lower left corner of the sources and will be referred to as the ¼ geometry, shown in Fig. 7. Because the ¼ geometry limited the azimuthal region of interest from 0-360° to 0-90°, the photopeak count rates for the ¼ geometry should be multiplied by four to imply the photopeak count rates for a full geometry. Overall, the ¼ geometry had the effect of increasing the source area by a factor of four without requiring multiple measurements of the area source.

Results and Discussion

Activity Measurements of the Buried Sources

Experiments were performed with buried area sources using the cylindrical NaI(Tl) detector and the experimental calibrations shown in Fig. 5. Referred to as experimental "setups," the three area sources of different ^{134}Cs activities were positioned in several arrangements with different absorber materials (aluminum, concrete, and plywood) and thicknesses between them. Measurements of the area source activities demonstrate the ability of collimation method to yield depth information.

Determining the Depth of a Buried Source and Comparison with other Methods

A simple, proof-of-principle experiment was performed to demonstrate the ability of collimation to yield depth information. Concrete bricks were stacked on top of the area source. The cylindrical NaI(Tl) detector was placed on the concrete layer, directly above the center of the area Source C. Measurements were taken using three concrete thicknesses: 9.2, 15.8, and 18.4 cm. For each concrete thickness, the 796 + 802 keV photopeak count rate was measured for an unshielded ("bare") detector and for a detector with the 0–34° collimator.

The ratio of the bare and collimated count rates is a function of the source depth in concrete. To establish the detector response relationships to the source depth, calculations of the uncollided gamma-ray flux at the detector were performed for an area source with the bare and collimated geometries using Eqs. (12) and (11), respectively. For a particular geometry, the uncollided gamma-ray flux depends on the activity and depth of the area source. However, the ratio of the two uncollided fluxes (measured as photopeak count rates) only depends on the depth of the area source because the source area activities cancel out. Fig. 8 displays the calculated bare-to-collimated response ratio for concrete thicknesses between 8 and 24 cm, as well as the measured values at depths of 9.2, 15.8, and 18.4 cm. Using the calculated response ratio in Fig. 8, the measurements of the bare and collimated count rates inferred the depth of the area source (i.e., thickness of the concrete layer). In general, good agreement in the measured and calculated results implies accurate predictions of the source depth. The measured depths are compared to actual source depths in Table 4. For the collimation method, the depth of the area source was predicted within 6% of its actual value for all three depths. As the concrete thickness increases, the measured photopeak count rates decreased due to increased gamma-ray attenuation and the

uncertainty in the measured response ratio increased due to counting statistics. Reduction in the counting uncertainties can be made at the expense of longer count times.

A comparison was made with the multiple photopeak and the peak-to-valley methods for determining depth information. Based on the measured data, predictions of the depth of the area source from these methods are displayed in Table 4. Because the energy resolution of the NaI(Tl) detector was not able to separate the 563, 569 and 605 keV photopeaks, the multiple photopeak method for ^{134}Cs was based on the ratio of the 796 + 802 keV photopeak count rate with the 563 + 569 + 605 keV summation photopeak. The multiple photopeak method predicted the three depths within 20%, where each actual depth was contained within the range of the 1σ uncertainties due to counting statistics. Based on the calibration procedure of Zombori et al. [12], the peak-to-valley method was the least successful and predicted the three area source depths within 61%. Although the uncertainty ranges were the largest for the peak-to-valley method, the actual source depth was outside the 1σ uncertainty range for the shallowest and deepest depths.

By using concrete, the experiments were not affected by large variations in the gamma-ray attenuation coefficient, which may be typical of heterogeneous environment situations due to changes in the soil moisture content and density. This challenge can be overcome by using the collimation method to determine the depth distribution of natural radionuclides, which tend to be more uniformly distributed. The depth distribution of the natural radionuclides could be used to infer changes in the gamma-ray attenuation coefficient with soil depth. Hence, the nonuniformities in the soil density can be deduced from the changes in the gamma-ray attenuation coefficient.

Activity Determinations of Two Area Sources at Different Depths

An experiment was designed to demonstrate the ability of the collimation method to determine the activities of two area sources buried at different depths in concrete from measurements using two collimators. As shown in Fig. 9, Source B was placed behind 9.2 cm of concrete and Source A was placed behind an additional 9.2 cm of concrete. The 0-34° collimator measurement yielded a photopeak count rate of 649 min^{-1}, and the 60-70° collimator measurement yielded a photopeak count rate of 9.98 min^{-1}. Solving Eqs. (15) and (16) for s_1 and s_2 yields 147 kBq and 609 kBq (3.98 μCi and 16.5 μ Ci), respectively, which compare very well to the actual source activities of 144 ± 16 kBq and 586 ± 37 kBq (3.89 ± 0.42 μ Ci and 15.8 ± 1.0 μ Ci), respectively. The presented uncertainties in the actual activities of the area sources are estimated 2σ values. In conclusion, the measured activities were within 4% of the actual activities and well within the uncertainties in the actual activities.

Activity Determinations of Three Area Sources at Different Depths

Two experiments (Setups 1 and 2) were conducted to demonstrate the ability to predict the activities of three area sources buried at deeper depths in concrete, aluminum, and wood from measurements using three collimators (0-34°, 42-60°, and 60-70°). As shown in Fig. 10 (a) and (b) for Setups 1 and 2, respectively, the three area sources were positioned at depths corresponding to an equivalent attenuation encountered in the upper 25 cm of soil. Where the two-source case was described by Eqs. (15) and (16), a system of three equations for the measured photopeak count rates with three source activity unknowns arises. A least-squares solution of the system of three equations was employed with a non-negative activity constraint. The results for Setups 1 and 2 are presented in Fig. 11 (a) and (b).

Throughout the this paper, the uncertainties in the measured activities were estimated values due to a 5% uncertainty applied to the each collimator's efficiency. For instance, factors of 0.95 or 1.05 were multiplied to each collimator's efficiencies for all three source locations and new reconstructions were performed. The minimum and maximum measured activities for each source were chosen from all combinations of the 0.95 and 1.05 multiplication factors on the collimator efficiencies. These worst case ranges in activity became the estimated uncertainties for the measured activities.

Overall, the measured activities were in good agreement with the actual activities. For Setup 1, the shallow and middle source activities were determined within 8%. However, the deepest source activity was overestimated by a factor of 1.4. For Setup 2, the shallow and middle source activities were determined within 14%. However, the weakest source, Source C, (at the greatest depth, equivalent to roughly 25 cm of soil) was located beneath the more active Sources A and B at shallower depths and was assigned a zero activity. In comparison to the counting statistics of Setup 2, the expected count rate from the weakest source was 2.8 times higher than the 1σ counting statistics for the 0-34° collimator measurement. However for the weakest source at the deepest location in Setup 2, the counting statistics were roughly 2 times greater than the expected count rate from the weakest source for the 42-60° collimator measurement. Because the activities of the middle and deepest sources were determined from the 0-34° and 42-60° collimator measurements, counting statistics could be a significant factor in the zero activity determination for the weakest source at the deepest location. In general for the two deep source arrangements in Setups 1 and 2, the greatest deviations from the actual activities occurred for the deepest source location.

Additionally, another experiment (Setup 3) buried the three area sources at shallower depths in concrete, aluminum, and wood. The three sources for experimental Setup 3 were positioned at depths equivalent to the gamma-ray attenuation of the upper 13 cm of soil and are depicted in Fig. 10(c). Shallow cases like Setup 3, could be used to test the spatial resolution of the collimation method (ie., the ability to "resolve" or assign non-zero activities to each of the three sources with less attenuating material separating them).

Due to the shallow nature of the Setup 3, an additional measurement using the 70-80° collimator was added to the 0-34°, 42-60°, and 60-70° collimator measurements and proved beneficial and allowed for an assessment of an overdetermined situation (four collimated measurements for three sources). For the overdetermined cases, a system of four equations for the measured photopeak count rates with three source activity unknowns arose. Again, a least-squares solution for the source activities was employed with a non-negative activity constraint. The results for Setup 3 are presented in Fig. 12. For Setup 3, the measured activities agreed very well (all within 18%) with the actual activities.

Description of the Reconstruction Process

Throughout this section, the reader may find it beneficial to refer to the Theory section for descriptions and relationships of the *in situ* calibration factors. Based on the measured N/ϕ data and calculated ϕ/S_A values, values for the total calibration factor (N/S_A) for each collimator were calculated for each source in a particular setup. The N/S_A values (equivalent to the product of the source area and the gamma-ray counting efficiency for the source) are tabulated in Table 5. Because the areas of the three sources were the same, greater N/S_A values correspond to greater counting efficiencies. In Setups 1 and 2, three measurements were taken of the three

sources. In Setups 3 and 4, four measurements were taken of the three sources. In all four setups, the source activities were determined from Eq. (18) to minimize the sum of the squares of the difference in the measured and calculated count rates divided by the measured count rate for each collimator. The minimizing calculations were perfromed with a spreadsheet solver[2], and a non-negative activity constraint was applied to all reconstructions. Assessment of the N/S_A calibration factors for a particular measurement geometry or setup allowed for improvements in the reconstruction results.

At times, the straightforward solution of the system of equations for the acquired measurement data resulted in zero activity predictions for the weaker sources. Instead of the straightforward approach of simultaneously solving the system of response equations, improved solutions were realized if the small N/S_A values, compared to others for a particular collimator measurement, could be avoided. The process of omitting the small contributions for certain source locations is referred to as "simplifying" the system of response equations. In general, the N/S_A calibration factors are calculated for known and unknown source distributions. Therefore, the assessment of the N/S_A calibration factors and simplification of the response equations do not require any additional *a priori* knowledge. The thought process behind the simplification of the response equations (ie, omission of the small N/S_A values) and specifics of the simplifications for each setup are described below.

Setup 1, shown in Table 5(a): The 60-70° collimator measurement of Setup 1 is dominated by the shallowest source ($N/S_A = 17.8$), while the deeper two sources contribute very little to the photopeak count rate ($N/S_A = 0.39$ and 0.01, respectively). Therefore, the dependency of the 60-70° collimator response was reduced to only the shallowest source (effectively the N/S_A values

for the middle and deepest sources were set to zero for the 60-70° collimator). Examining the N/S_A values for the 42-60° collimator reveals that the $N/S_A = 0.23$ for deepest source is much smaller than the other sources (less than 100 times smaller than the shallowest source and less than 10 times smaller than the middle source). Therefore, the dependency of the 42-60° collimator response was reduced to the shallowest and middle source. In other words, the activity of the deepest source was determined from the collimated measurement where its contribution was the most significant, namely 0-34°. After these adjustments, the system of three equations was solved simultaneously. To better show the simplification of the response equations, Eq. (21) displays the system of three response equations for Setup 1 and highlights the three omitted terms:

$$
\begin{aligned}
R(0-34°) &= \left(0.587\frac{cph}{\gamma/s}\right)\cdot s_1 + \left(0.125\frac{cph}{\gamma/s}\right)\cdot s_2 + \left(0.026\frac{cph}{\gamma/s}\right)\cdot s_3 \\
R(42-60°) &= \left(0.142\frac{cph}{\gamma/s}\right)\cdot s_1 + \left(0.014\frac{cph}{\gamma/s}\right)\cdot s_2 + \cancel{\left(0.001\frac{cph}{\gamma/s}\right)\cdot s_3} \\
R(60-70°) &= \left(0.104\frac{cph}{\gamma/s}\right)\cdot s_1 + \cancel{\left(0.002\frac{cph}{\gamma/s}\right)\cdot s_2} + \cancel{\left(0.00006\frac{cph}{\gamma/s}\right)\cdot s_3}
\end{aligned}
\qquad (21)
$$

where the R terms represent the measured photopeak count rates with the different collimator and the s_i terms represent the gamma-ray emission rate for the i^{th} area source.

Setup 2, shown in Table 5(b): The 60-70° collimator measurement of Setup 2 is also dominated by the shallowest source ($N/S_A = 0.662$), while the deeper two sources contribute very little to

photopeak count rate (N/S_A = 0.013 and 0.007, respectively). Therefore, the dependency of the 60-70° collimator response was reduced to only the shallowest source. However for the 42-60° collimator, the N/S_A = 0.215 for deepest source is close in magnitude to N/S_A = 0.312 for the middle source. Therefore, the solution for the response of the 42-60° collimator was unaltered and remained dependent on all three of the sources. Again, the system of three equations was solved simultaneously.

Setup 3, shown in Table 5(c): In Setup 3, a 70-80° collimator measurement was added for a total of four collimator measurements of the three sources. The 70-80° collimator measurement was dominated by the shallowest source (N/S_A = 4.71), while the deeper two sources accounted for smaller contributions (N/S_A = 0.71 and 0.01, respectively), and the dependency of the 70-80° collimator response was reduced to only the shallowest source. The dependency of the 60-70° collimator response was also reduced to only the shallowest source. The 60-70° and 70-80° collimator measurements were coupled to determine the activity of the shallowest source. The dependency of the 42-60° collimator response was reduced to the shallowest and middle source, while the 0-34° collimator remained dependent on all three of the sources. Having already solved for the activity of the shallowest source, the system was reduced to two equations and two unknowns, which were then solved simultaneously based on the measured 0-34° and 42-60° data.

Deep Source Correction

Measurements with the 0-34° collimator of a single area source beneath at least 9.2 cm of concrete indicated that the N/S_A calibration factor was slightly underestimated by a factor of 1.07

for these deeper source locations. The 1σ uncertainties due to counting statistics for these measurements ranged between 1.1 and 4.4% could partially account for the 7% correction factor. Perhaps, the effect of the uncertainty in the linear attenuation coefficient for concrete was magnified in the N/S_A calibration factor for deeper source locations (refer to the uncertainty analysis in Chapter IX of Benke [25]). Since the only significant difference in the measured and calculated N/S_A was found with the 0-34° collimator for deeper source locations, a correction factor of 1.07 (determined from actual measurements of an area source beneath at least 9.2 cm of concrete) was multiplied to the calculated N/S_A of the 0-34° collimator for those sources behind at least 9.2 cm of concrete-equivalent attenuation and will be referred to as the deep source correction. The value of deep source correction factor was determined from actual measurements of an area source beneath at least 9.2 cm of concrete.

Except for Setup 2, the deep source correction had the effect of reducing the activity of the deepest source by less than 11%, which resulted in a better agreement between the measured and actual source activities. In Setup 2 the three area sources were positioned behind the largest amount of concrete. In fact, Setup 2 was the only arrangement where all three sources were behind at least 9.2 cm of concrete. Therefore, it is not surprising that deep source correction had a greater effect on the results for Setup 2. Without the deep source correction, all of the activity was assigned to Source A, the most active source at the shallowest position. Employing the correction allowed for the identification of Source B, behind 18.4 cm of concrete and 1.2 cm of wood.

Impact of Removing Collimated Measurements

For Setup 3 consisting of the three buried sources, four collimated measurements were acquired to yield an overdetermined situation. To access the effect of taking an extra measurement, the photopeak count rate data were reanalyzed excluding one of the collimated measurements and the results are displayed in Table 12. For Setup 3, omission of the 70-80° collimator data resulted in a slightly worse activity determination. The middle source's activity prediction changed from a 3.3% underestimation (well within the uncertainty range of the actual activity) to a 50% overestimation. However, the weakest source, Source C, was still resolved (ie., assigned a non-zero activity) in between the other two sources.

Distributed Source Reconstructions

The collimation method was also used to determine the depth distribution in a different fashion, which involved the division of the source medium into several depth layers. Referred to as "distributed source reconstructions," depth distributions were ascertained by determining the source activities within each depth layer for measurement Setup 1. Although area sources were used in the measurement setups, activity reconstructions were performed for independent depth layers with a uniform radionuclide distribution (instead of determining the activities of area source at different depths). Throughout this paper, the term "sectioning scheme" refers to how the source medium was divided into depth layers. Different sectioning schemes imply different depth layer thicknesses and/or materials for the same measurement setup and area source arrangement.

For the case of activity reconstructions of the buried area source, the depths of the area sources were used in the calculations of the gamma-ray counting efficiencies with each

collimator. Using the depth information of the area sources for the detector efficiency calculations does not represent a limitation of this approach for the following reason. Before the measurement and analysis of the radionuclide depth distribution within a volume source, the volume source must be divided into depth layers to allow for the calculation of detector efficiencies for each depth layer. The process of dividing a volume source into layers of finite thicknesses defines the depth of each source layer. In general, the thicknesses of the source layers can be chosen in any fashion to best characterize each specific situation (ie., the chosen layers do not need to have equal thicknesses and can contain more than one material). Even for those situations where the actual source distributions are close to a planar distribution, such as contamination at the surface of a floor/wall or underneath/behind layers of uncontaminated material, *a priori* information about the area source depth is not required because the floor/wall would be divided into depth layers. Subsequent *in situ* measurements would determine the radionuclide activities contained within each depth layer.

The area source geometries were also used to simulate sources distributed with depth. However, instead of calculating counting efficiencies for specific source depths, counting efficiencies were calculated for several depth layers with uniform radionuclide distributions. By sectioning the source geometry into depth layers, the need for the *a priori* selection of a function for the radionuclide depth distribution is alleviated. The reconstructions of the collimated measurements now determine the amount of activity contained within each depth layer, rather than the activity of the individual sources. Because the fabricated collimators did not limit the azimuthal field of view, a uniform spatial distribution of radionuclide was assigned to each depth layer. Although other depth distributions within each depth layer could be used in conjunction

with the uniform spatial distribution, the radionuclide depth distribution within each depth layer was also defined to be uniform in this work.

The three-source geometry of Setup 1, displayed in Fig. 10(a), was used to demonstrate the ability of the method to predict the amount of activity contained within each depth layer. For the distributed source reconstructions, the source geometries were simplified to consist only of aluminum and concrete. In this section, the presence of wood in the measurement setups was only accounted for in the attenuation calculations of the deepest layer. In the case of Setup 1, the source geometry was reduced to a 0.95-cm aluminum plate in front of 23 cm of concrete and was divided into three layers as depicted in Fig. 13(a). The first depth layer was chosen to incorporate the materials at the depths of 0 – 2.95 cm and consisted of an aluminum thickness of 0.95-cm above 2 cm of concrete. The second depth layer consisted entirely of concrete at the depths of 2.95 – 11.95 cm, and the third depth layer accounted for the concrete at the depths of 11.99 – 23.95 cm.

For the distributed source reconstructions using the experimental calibrations, the total *in situ* calibration factors, N/S_A, for each depth layer and collimator were calculated from Eq. (20). The measurements and reconstruction procedures for the distributed source case were performed in the same manner as initially done for Setup 1. Based on the same 0–34°, 42–60°, and 60–70° measurement data, the determinations of the activities contained within each depth layer are presented in Fig. 14. For this particular sectioning scheme, the largest discrepancy from the actual activities arose in the middle layer, where the activity was underestimated by a factor of 1.9. The underestimation of the middle layer's activity can be partially accounted for by the relative location of the actual area source within the depth layer. In this case, the location of Source B was at the very bottom of the middle layer. Therefore, the calculated efficiency for the

middle layer is greater than the counting efficiency of the area source. For the same measured photopeak count rate, an increase in efficiency implied a smaller activity determination. Source A was located closer to the center of the deepest layer and did not experience such a large discrepancy from the actual activity. Although the sectioning of source geometries was somewhat arbitrary, multiple reconstructions from a single set of collimated measurements could be performed for different sectioning schemes.

To reduce the effect of large efficiency deviations due to source locations near the top or bottom of the depth layers, a new "centered" sectioning scheme located the area sources in the middle of the depth layers as shown in Fig. 13(b). A new "centered" distributed source reconstruction was determined from the "centered" sectioning scheme. Because the shallowest depth layer consisted of aluminum and concrete, the middle of the layer was determined from the weighting the thickness of the materials with their gamma-ray attenuation coefficient. Setup 1 was sectioned into layer thicknesses of 0.95 cm of aluminum plus 1.20 cm of concrete, 17 cm concrete, and 4.78 cm of concrete, respectively for increasing depths.

The activity determinations for the new "centered" sectioning scheme are listed in Fig. 14. Compared to the actual source activities, "centering"of the area sources improved the middle layer's activity determination from a –49% percent difference to –14%. However, the discrepancies from the actual activities for the other two layers increased after "centering," and resulted in the largest percent difference of +72% at the deepest layer. Recall that the activity reconstructions typical exhibited the largest deviations from the actual activities at the deepest source location. Therefore, it is not surprising that "centering" the area sources within the depth layers caused the results of the distributed source reconstructions to behave more like the activity reconstructions of the individual sources. The analysis where the area sources were not centered

within the depth layers illustrates the capability of the collimation method for determining depth distributions without *a priori* knowledge of the source locations.

Conclusions

To test the ability of the presented method to determine depth information, area sources were created and placed at various depths in attenuating materials. The collimation method was implemented on a NaI(Tl) detector with experimental calibrations. Overall when compared to the other *in situ* methods (multiple photopeak and peak-to-valley methods), the collimation method exhibited the greatest accuracy for determining the depth of a single area source, as well as the smallest uncertainties. It is important to note, that this simple experiment required the determination of a single quantity (ie., the source depth). As the complexity of the experiments using the NaI(Tl) detector were increased to include multiple area sources, multiple depth quantities had to be determined. However, the multiple photopeak and the peak-to-valley methods were limited to determining a single depth quantity. Therefore, further comparisons with the other methods for the more complex experiments using the NaI(Tl) detector were not possible.

For the presented experimental setups of two or three area sources located at different depths, the collimation method determined the area source activities of the upper (shallower) two area sources to within 15% of their actual activities. Only for the setup with the weakest source at the deepest location were the counting statistics significant enough to be considered a factor in the zero activity determination. In general, the greatest deviations from the actual source activities occurred for the deepest source locations, which was expected because the determinations of the deepest source activity are strongly dependent on the activity determinations of the shallower sources. When the activities of the three area sources were

determined from four collimated measurements instead of three measurements, those overdetermined situations improved the determinations of the area source activities.

To obtain distributed source reconstructions, the collimation method was applied with an approach that divided the source medium into several depth layers. The depth distributions were ascertained by determining the source activities within each depth layer. Although area sources were used in the measurement setups, activity reconstructions were performed for independent depth layers with a uniform radionuclide distribution (instead of determining the activities of area source at different depths). The relative depth location of the area sources within the depth layers affected the gamma-ray counting efficiencies and could be responsible for significant deviations (because the representation of the source geometry differs so much from the actual setup used in the comparisons). Therefore, the distributed source reconstructions presented should be considered as less than ideal applications of the collimation method. In general, radionuclides tend to be much more widely distributed in most field environments where no depth distribution information is available. In these more common situations, the distributed source reconstructions become more applicable. It is important to note that the area sources were not required to be located in the middle of the depth layers to obtain good agreement with the actual activities. Overall, the collimation method preserved the qualitative shapes of the actual depth distributions for each of experimental setups (even for non-monotonic depth distributions).

While the measurement results of other *in situ* methods only have the ability of determining a single depth parameter in general, the number of depth parameters quantified by the collimation method increases with the number of collimated measurements. An exception exists if the radionuclide of interest emits three or more significant gamma-rays, appreciably separated in energy, and if the spectrometer used has sufficient energy resolution to identify and

separate each gamma-ray emission. In such cases, the multiple photopeak method could determine one fewer number of depth parameters than the number of significant gamma-ray emissions. As an example, the subsurface maxima exhibited by aged ^{137}Cs fallout in soil are best described by at least two depth parameters and can not be adequately characterized by a single depth parameter. The measurements of the activities of area sources buried in attenuating materials demonstrated the ability of the collimation method to accurately determine radionuclide depth distributions for soil-equivalent depths up to 25 cm. Since over 95% of the ^{137}Cs contamination typically resides in the upper 25 cm of soil, the collimation used is well suited for determining depth distributions of ^{137}Cs in soil [25].

In conclusion, the collimation method represents an improvement over conventional *in situ* methodologies by offering these additional benefits:

- Does not require soil sampling to determine a distribution function
- Does not require the *a priori* selection of a depth distribution function (instead reconstructs the depth distribution with a histogram approach)
- Only requires the analysis of a single gamma-ray emission
- Provides a more detailed and accurate distribution information
- Offers a superior ability for characterizing complex depth distributions

Based on the results of actual measurements, the ability of the presented collimation method to determine radionuclide depth distributions increases the potential of *in situ* gamma-ray spectrometry as an independent characterization tool.

Acknowledgements

Charlie Weger machined the lead collimators used in this research, and his efforts are greatly appreciated. The authors are also grateful to Dr. David Hamby for the use of his NaI(Tl) spectroscopy system and laboratory space. Joe Miklos deserves recognition for his assistance with the creation of the area sources. Phil Simpson's immediate attention to questions and willingness to help was also appreciated. Dr. James Holloway, Dr. Zhong He, Dr. Avery Demond, and Dr. Ronald Fleming are thanked for their suggestions. This research was performed under appointment to the Civilian Radioactive Waste Management Fellowship program administered by the Oak Ridge Institute for Science and Education under contract number DE-AC05-76OR00033 between the U.S. Department of Energy and the Oak Ridge Associated Universities.

References

[1] L. R. Anspaugh, IEEE Trans. Nucl. Sci. NS-23, 3 (1976) 1190-1196.

[2] W. Sowa, E. Martini, K. Gehrcke, P. Marschner, M. J. Naziry, Radiat. Prot. Dosim. 27, 2 (1989) 93-101.

[3] S. H. Fong, J. L. Alvarez, Health Phys. 72, 2 (1997) 286-295.

[4] J. MacDonald, C. J. Gibson, P. J. Fish, D. J. Assinder, J. Radiol. Prot. 17, 1 (1997) 3-15.

[5] L. L. Gadeken, M. L. Gartner, D. E. Sharbak, D. F. Wyatt, The Log Analyst 32, (1991) 24-34.

[6] L. L. Gadeken, H. D. Smith Jr., The Log Analyst 28, 1 (1987) 27-36.

[7] L. L. Gadeken, H. D. Smith, Jr., Seifert, D. J. The Log Analyst 29, 3 (1988) 159-177.

[8] M. Korun, R. Martinčič, B. Pucelj, Nucl. Instrum. Methods Phys. Res. A 300 (1991) 611-615.

[9] K. Rybacek, P. Jacob, R. Meckbach, Health Phys. 62, 2 (1992) 519-528.

[10] K. M. Miller, P. Shebell, G. A. Klemic, Health Phys. 67 (1994) 140-150.

[11] E. P. Naessens, X. G. Xu, Health Phys. 77, 1 (1999) 76-88.

[12] P. Zombori, A. Andrási, I. Németh, A new method for the determination of radionuclide distribution in the soil by in situ gamma-ray spectrometry. Budapest, Hungary: Central Research Institute for Physics, Institute for Atomic Energy Research. KFKI-1992-20/K, 1992.

[13] A. N. Tyler, D. C. W. Sanderson, E. M. Scott, J. Environ. Radioactivity 33, 3 (1996) 195-212.

[14] A. N. Tyler, J. Environ. Radioactivity 45 (1999) 235-252.

[15] A. V. Chesnokov, V. I. Fedin, A. P. Govorun, O. P. Ivanov, V. I. Liksonov, V. N. Potapov, S. V. Smirnov, S. B. Shcherbak, L. I. Urutskoev, Appl. Radiat. Isot. 48, 9 (1997) 1265-1272.

[16] V. N. Golosov, D. E. Walling, E. V. Kvasnikova, E. D. Stukin, A. N. Nikolaev, A. V. Panin, J. Environ. Radioactivity 48 (2000) 79-94.

[17] M. Korun, A. Likar, M. Lipoglavšek, R. Martinčič, B. Pucelj, Nucl. Instrum. Methods Phys. Res. B 93 (1994) 485-491.

[18] J. MacDonald, C. J. Gibson, P. J. Fish, D. J. Assinder, IEEE Trans. Nucl. Sci. 46, 3 (1999) 424-428.

[19] H. L. Beck, J. De Campo, C. V. Gogolak, In situ Ge(Li) and Na(Tl) gamma-ray spectrometry. New York: US Department of Energy, Environmental MeasurementsLaboratory. HASL-258, 1972.

[20] I. Németh, E. Lovranich, E. Urbanich, P. Zombori, A. Andrási, F. Steger, Calibration of a HP-germanium detector for rapid in-situ determination of environmental radioactivity. Seiberdorf, Austria: Österreichisches Forschungszentrum, Institute für Strahlenschutz. OEFZS—4461, ST—1160/88, 1988.

[21] K. M. Miller, P. Shebell, *In situ* gamma-ray spectrometry – A tutorial for environmental radiation scientists. New York: US Department of Energy, Environmental Measurements Laboratory. EML-557, 1993.

[22] M. Abramowitz, I. A. Stegun, Handbook of Mathematical Functions. New York, NY: Dover Publications, Inc., 1972, pp. 228-229.

[23] J. R. Lamarsh, Introduction to Nuclear Engineering. Second ed., Reading, MA: Addison-Wesley Publishing Company, 1983.

[24] Bureau of Radiological Health, Radiation Health Handbook. Washington, D.C.: U.S. Government Printing Office, 1970.

[25] R. R. Benke, An improved method for determining radionuclide depth distributions using *in situ* gamma-ray spectrometry. Ph.D. Dissertation, The University of Michigan: Ann Arbor, MI, 2000.

Footnotes

[1] EG&G Instruments, Inc., 100 Midland Road, Oak Ridge, TN 37831-0895. EG&G Ortec is registered trademark of EG&G Instruments, Inc.
NaI(Tl) Spectroscopy System Components:
NaI(Tl) detector, EG&G Ortec, Catalog #905-4, Type S-1212, Serial #E5402
Photomultiplier and Preamplifier, EG&G Ortec #276
NIM Bin, EG&G Ortec #4001A
High Voltage Supply, EG&G Ortec #478
Amplifier, EG&G Ortec#575A
EG&G Ortec Multichannel Analyzer card for an IBM-compatible desktop computer
MEASTRO™ for Windows 3 Counting Software, EG&G Ortec, Version 2.03

[2] Excel 97. Microsoft Corporation, 1 Microsoft Way, Redmond, WA 98052

Table 1. General advantages and disadvantages of the three standard *in situ* methods for determining radionuclide depth distributions.

Method	Advantages	Disadvantages
Multiple Photopeak	requires a single measurement at each site	requires at least two significant gamma-ray emissions
		gamma-ray emissions must have a large separation in energy
		depth information limited by the gamma-ray decay scheme of the radionuclide of interest
		multiple measurements at the same site yield no additional depth information
Peak-to-Valley Ratio	requires only one significant gamma-ray emission	sensitive to interference in complex gamma-ray fields
	requires a single measurement at each site	multiple measurements at the same site yield no additional depth information
Lead Plate	requires only one significant gamma-ray emission	requires multiple measurements at each site
	multiple measurements at the same site yield additional depth information	adds weight to the portable system

Table 2. Significant gamma-ray emissions for ^{134}Cs.

Energy (keV)	Yield (%)
475.4	1.46
563.2	8.38
569.3	15.4
604.7	97.6
795.9	85.4
802.0	8.73
1038.6	1.00
1167.9	1.80
1365.2	3.04

Table 3. Activities for the ^{134}Cs area sources. The area source activities were decay corrected for the comparisons with the measured activities. The 2σ uncertainties presented were estimated from uncertainties in measured photopeak count rates due to counting statistics, the angular response of the detector, geometrical representation of the area source, and nonuniformities in the area source activity.

Source A	579 ± 36 kBq	(15.7 ± 0.98 μCi)
Source B	142 ± 15 kBq	(3.84 ± 0.42 μCi)
Source C	31 ± 3.3 kBq	(0.83 ± 0.09 μCi)

Table 4. Measurements of the source depth in concrete for a planar radioactive source from *in situ* spectroscopic methods based on multiple photopeaks, and the peak-to-valley ratio, and the presented collimation technique. The numbers in parenthesis represent the impact of 1σ uncertainties arising from counting statistics on the calculated concrete thicknesses. Note that the uncertainties are asymmetrical about the calculated concrete thickness because the calculated ratio of Fig. 8, used to infer the source depth from the measured ratio, exhibited a nonlinear relationship.

Actual Thickness (cm)	Multiple Photopeak Method Thickness (cm)	Peak-to-Valley Method Thickness (cm)	Collimation Method Thickness (cm)
9.2	8.7 (8.2 – 9.3)	3.6 (3.1 – 4.1)	9.2 (8.9 – 9.5)
15.8	17.5 (15.1 – 20.2)	13.9 (11.7 – 17.0)	15.5 (14.2 – 17.1)
18.4	14.9 (11.4 – 19.1)	24.7 (20.5 – 30.8)	19.5 (16.9 – 22.7)

Table 5. Calculated N/S_A calibration factors for each source location of the three-source setups: (a) Setup 1, (b) Setup 2, and (c) Setup 3. For each of the four setups, the shallowest source is listed in the first row, the middle source is listed in the second row, and deepest source is listed in the third row.

(a) Setup 1 shown in Fig. 10(a)

	N/S_A (counts min^{-1} per γ s^{-1} cm^{-2})		
Source	0-34° Collimator	42-60° Collimator	60-70° Collimator
C	100.8	24.4	17.8
B	21.5	2.37	0.39
A	4.42	0.23	0.01

(b) Setup 2 shown in Fig. 10(b)

	N/S_A (counts min^{-1} per γ s^{-1} cm^{-2})		
Source	0-34° Collimator	42-60° Collimator	60-70° Collimator
A	26.8	3.27	0.662
B	5.47	0.31	0.013
C	4.25	0.22	0.007

(c) Setup 3 shown in Fig. 10(c)

	N/S_A (counts min^{-1} per γ s^{-1} cm^{-2})			
Source	0-34° Collimator	42-60° Collimator	60-70° Collimator	70-80° Collimator
B	100.8	24.4	17.8	4.71
C	61.5	13.3	6.45	0.71
A	22.0	2.42	0.38	0.01

Figure Captions

Fig. 1. Cross-sectional view of the *in situ* gamma-ray spectrometry setup with a lead plate located at two different distances from the detector. The detector predominately responds to those gamma-ray emitted from radionuclides located outside the dashed lines. (a) For a lead plate location close to the detector, the detector preferentially responds to those radionuclides contained within the shallower layers of soil. (b) For a large lead plate distance from the detector, the detector is shielded from those radionuclides located directly beneath the lead plate, and a larger volume of soil contributes to the detector response.

Fig. 2. Schematic view of the *in situ* gamma-ray spectrometry geometry with a planar source at a depth z in soil. In the following figure, θ is the off-axis polar angle of the radionuclide measured from the axis of the detector in units of radians, h is the height of the detector above the soil surface in units of cm, μ_s is the linear gamma-ray attenuation coefficient for soil in units of cm^{-1}, μ_a is the linear gamma-ray attenuation coefficient for air in units of cm^{-1}, r represents the radius of dA on the planar source, ρ is the distance from the detector to a radionuclide contained within an infinitesimal source area in units of cm, ρ_{air} is the path length in air with units of cm, and dA is an infinitesimal source area.

Fig. 3. Cross-sectional view of the collimator/detector geometry on the source surface. Those gamma-rays emitted within the collimated region of interest and within the polar angle range do not encounter collimator attenuation along their path to the center of the detector crystal and are preferentially detected (larger collimator thicknesses will further reduce contributions outside of the region of interest). Depiction of three gamma-ray trajectories: (a) photons emitted within the collimated region and incident on the detector within the polar angle range encounter no collimator attenuation, (b) photons emitted outside the collimated region and directed toward the detector within the polar angle range encounter lead attenuation, and (c) photons emitted within the collimated region and directed outside the polar angle range encounter collimator attenuation.

Fig. 4(a). Cross-sectional diagram of the dimensions for the 0-34° collimator. All dimensions are in centimeters.

Fig. 4(b). Cross-sectional diagram of the dimensions for the 42-60° collimator. All dimensions are in centimeters.

Fig. 4(c). Cross-sectional diagram of the dimensions for the 60-70° collimator. All dimensions are in centimeters.

Fig. 4(d). Cross-sectional diagram of the dimensions for the 70-80° collimator. All dimensions are in centimeters.

Fig. 5(a). Measured data and fitted polynomial of the area source detection efficiency for the 0-34° collimator as function of depth in air. The error bars presented represent 2σ values due to counting statistics.

Fig. 5(b). Measured data and linear fit of the area source detection efficiency for the 42-60° collimator as function of depth in air. The error bars presented represent 2σ values due to counting statistics.

Fig. 5(c). Measured data and linear fit of the area source detection efficiency for the 60-70° collimator as function of depth in air. The error bars presented represent 2σ values due to counting statistics.

Fig. 5(d). Measured data and fitted polynomial of the area source detection efficiency for the 70-80° collimator as function of depth in air. The error bars presented represent 2σ values due to counting statistics.

Fig. 6. Experimental setup for the full geometry: (a) top view and (b) side view including cross-sectional view of the collimator. The full geometry was used for the 0-34° collimator measurements.

Fig. 7. Experimental setup for the ¼ geometry: (a) top view and (b) side view including a cross-sectional view of the collimator. Note that when the count rate data obtained from measurements of the ¼ geometry are multiplied by four, it is equivalent to a measuring a source four times greater in area. The ¼ geometry allowed for more manageable sizes of the area sources (1.02 m by 1.02 m), reduced the amount of repetitive attenuating material, and consumed less laboratory space. The ¼ geometry was used for all collimator measurements except the 0-34° measurements.

Fig. 8. Calculated and measured bare-to-collimated response ratio versus concrete thickness. The calculated ratio was determined from Eqs. (12) and (11). The lead collimator reduced the detector field of view to 0-34°. The measured error bars represent the 1σ uncertainty due to counting statistics. Counting times for the bare and collimated geometries ranged from 6.9 to 15 h.

Fig. 9. Attenuating materials and source locations for the two-source measurements. The presented dimensions represent the material thickness. The wood thickness of each source layer is 0.5 cm.

Fig. 10(a). Attenuating materials and source locations for the three-source Setup 1. The presented dimensions represent the material thickness. For proper alignment and improved stability, Sources B and C were attached to larger plywood boards with a thickness of 1.2 cm. The wood thickness of each source layer is 0.5 cm.

Fig. 10(b). Attenuating materials and source locations for the three-source Setup 2. The presented dimensions represent the material thickness. Note the small amount of attenuating material between Sources B and C (equivalent to the attenuation for the 796 + 802 keV gamma-rays of only 1.8 cm of soil or 1.4 cm of concrete).

Fig. 10(c). Attenuating materials and source locations for the three-source Setup 3. The presented dimensions represent the material thickness. Note the small amount of attenuating material between Sources B and C (equivalent to only 2.8 cm of soil or 2.2 cm of concrete).

Fig. 11(a). Actual and measured activities of three area sources at different depths for Setup1 shown in Fig. 10(a). The area sources C, B, and A, respectively, were positioned at increasing depths from the surface. The measured activities were determined from three measurements with the 0-34°, 42-60°, and 60-70° collimators. The presented uncertainties in the measured activities are estimated values for the worst case results due to a 5% uncertainty applied to each collimator's efficiency. The presented uncertainties in the actual activities of the area sources are estimated 2σ values.

Fig. 11(b). Actual and measured activities of three area sources at different depths for Setup 2 shown in Fig. 10(b). The area sources A, B, and C, respectively, were positioned at increasing depths from the surface. The measured activities were determined from three measurements with the 0-34°, 42-60°, and 60-70° collimators. The presented uncertainties in the measured activities are estimated values for the worst case results due to a 5% uncertainty applied to each collimator's efficiency. The presented uncertainties in the actual activities of the area sources are estimated 2σ values.

Fig. 12. Actual and measured activities of three area sources at different depths for the Setup 3. Shown in Fig. 10(c), the area sources B, C, and A, respectively, were positioned at increasing depths from the surface. The "3 Measurements" case used the NaI(Tl) detector with the 0–34°, 42-60°, and 60–70° collimators. The "4 Measurements" case added a 70–80° collimator measurement. The presented uncertainties in the measured activities are estimated values for the worst case results due to a 5% uncertainty applied to each collimator's efficiency. The presented uncertainties in the actual activities of the area sources are estimated 2σ values.

Fig. 13(a). Simplification of Setup 1, shown in Fig. 10(a), for the distributed source reconstructions and sectioning into three depth layers. Depth layer 1 consisted of an aluminum thickness of 0.95 cm and a concrete thickness of 2.0 cm. Depth layers 2 and 3 consisted of concrete thicknesses of 9.0 and 12 cm, respectively.

Fig. 13(b). Sectioning Setup 1 into depth layers with the area sources "centered" within the layers. Depth layer 1 consisted of an aluminum thickness of 1.0 cm and a concrete thickness of 0.95 cm. Depth layers 2 and 3 consisted of concrete thicknesses of 17.0 and 4.8 cm, respectively.

Fig. 14. Actual and measured activities for the distributed source reconstructions of the three-source Setup 1 in Fig. 10(a). The distributed source reconstructions were based on NaI(Tl) detector measurements with the 0–34°, 42–60°, and 60–70° collimators. Two sectioning schemes were employed: (a) for depth layers consisting of 0.95 cm of aluminum plus 2 cm of concrete, 9 cm of concrete, and 12 cm of concrete, respectively at increasing depths, and (b) where the area sources were "centered" within the depth layers, corresponding to 0.95 cm of aluminum plus 1.2 cm of concrete, 17.0 cm of concrete, and 4.78 cm of concrete, respectively at increasing depths. The presented uncertainties in the measured activities are estimated values for the worst case

results due to a 5% uncertainty applied to each collimator's efficiency. The presented uncertainties in the actual activities of the area sources are estimated 2σ values.

(a)

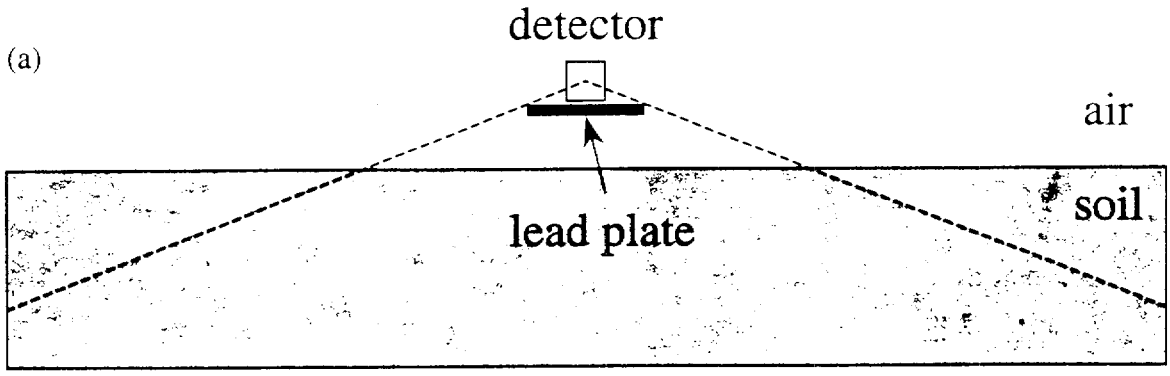

(b)

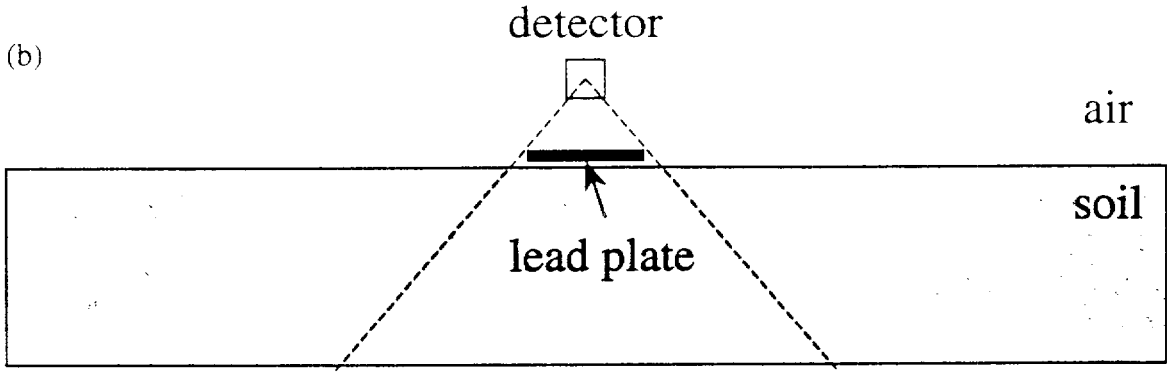

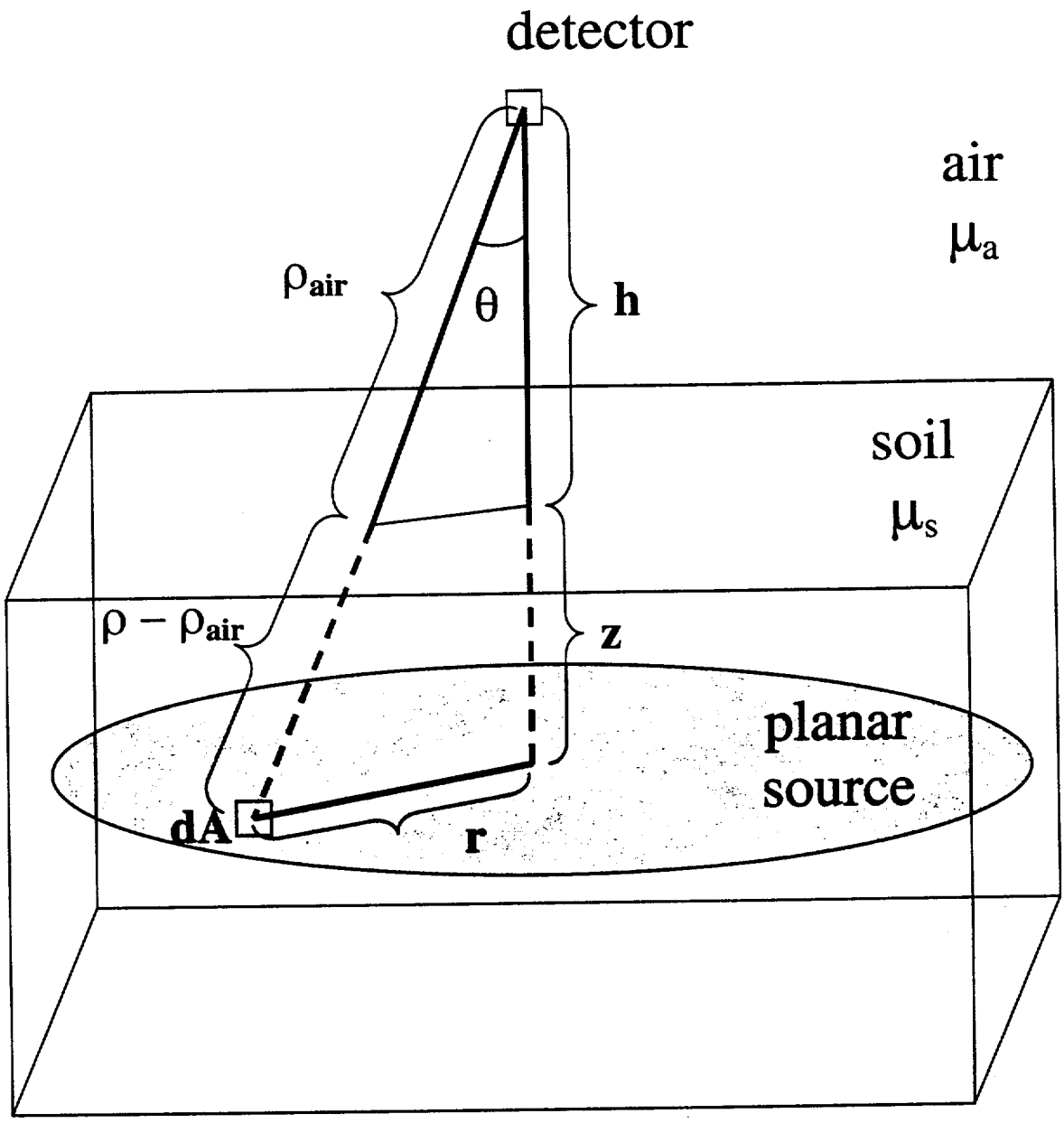
detector
air
μ_a
ρ_{air}
θ
h
soil
μ_s
$\rho - \rho_{air}$
z
planar
source
dA
r

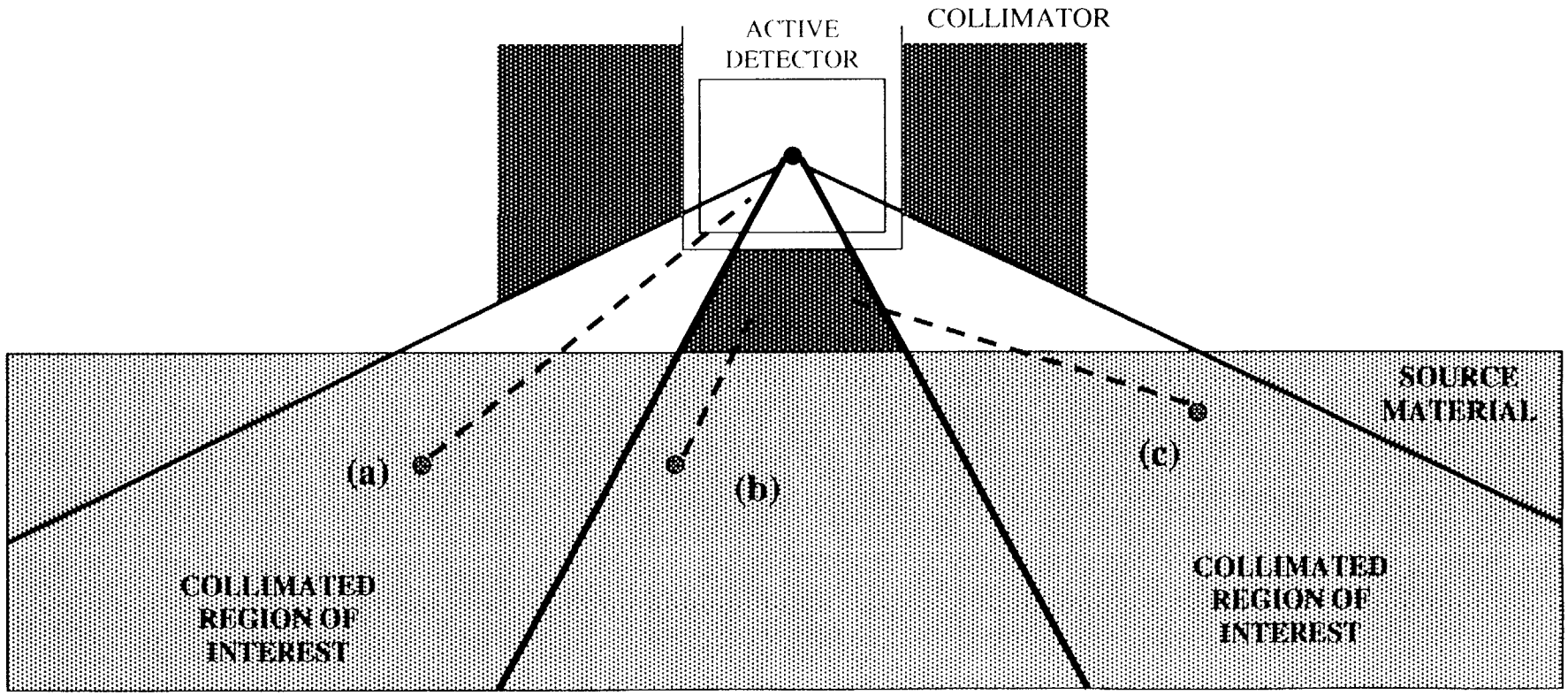
ACTIVE
DETECTOR
COLLIMATOR
SOURCE
MATERIAL
(a)
(b)
(c)
COLLIMATED
REGION OF
INTEREST
COLLIMATED
REGION OF
INTEREST

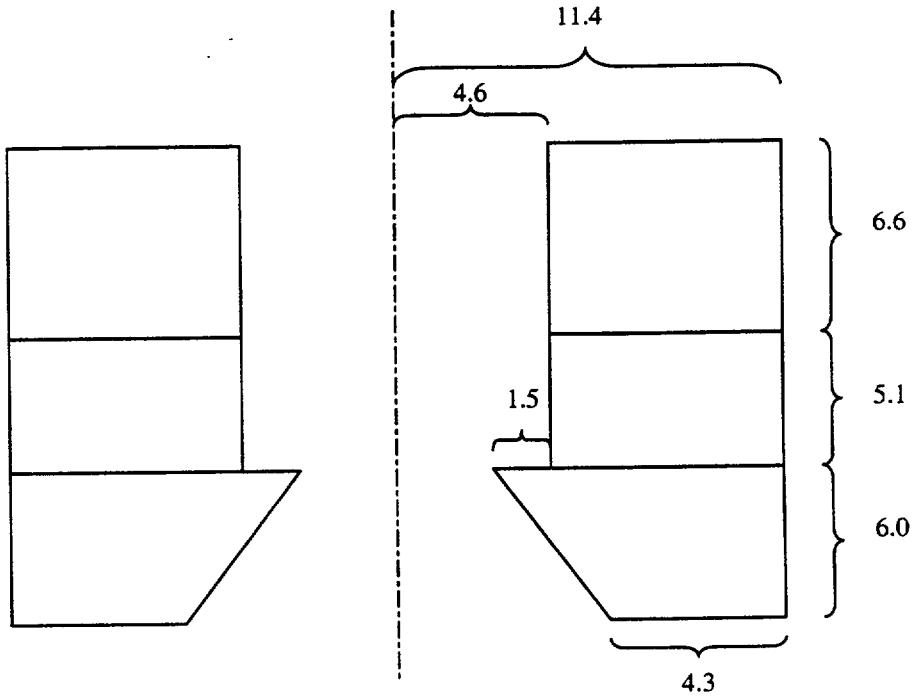
11.4
4.6
6.6
5.1
1.5
6.0
4.3

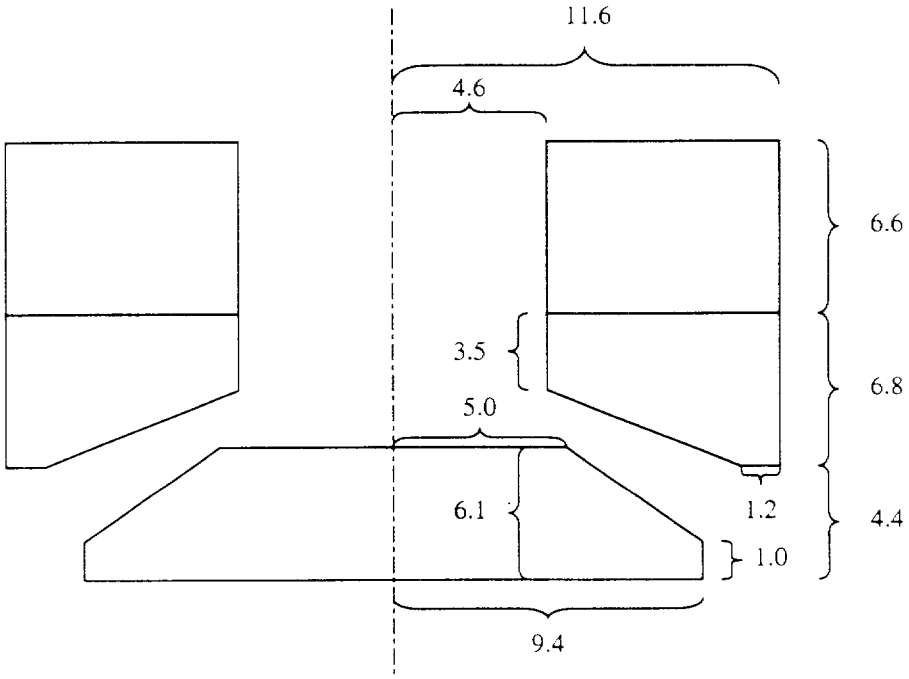
11.6
4.6
6.6
3.5
6.8
5.0
6.1
1.2
4.4
1.0
9.4

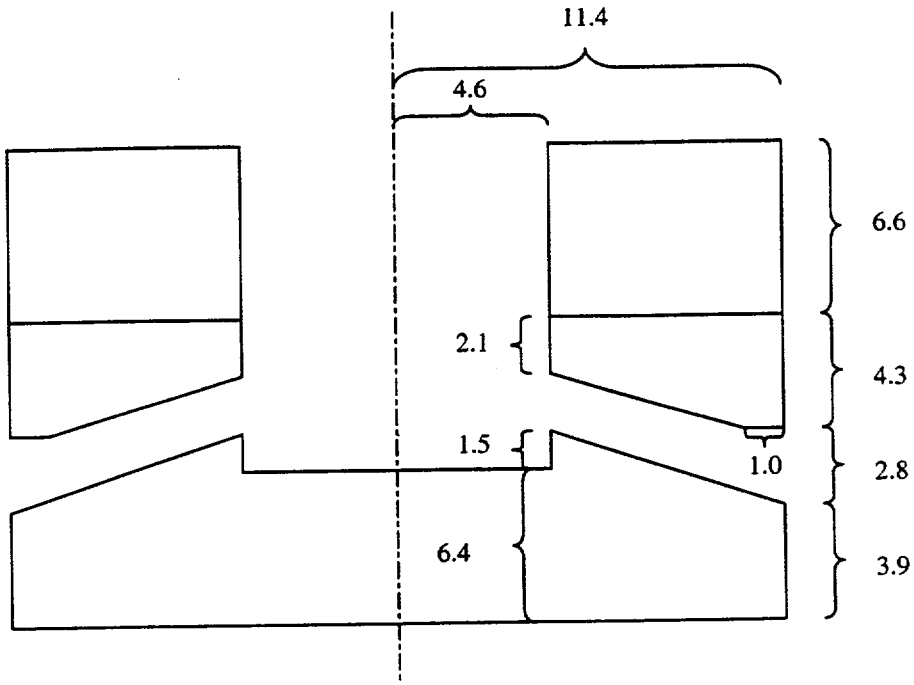
11.4
4.6
6.6
2.1
4.3
1.5
1.0
2.8
6.4
3.9

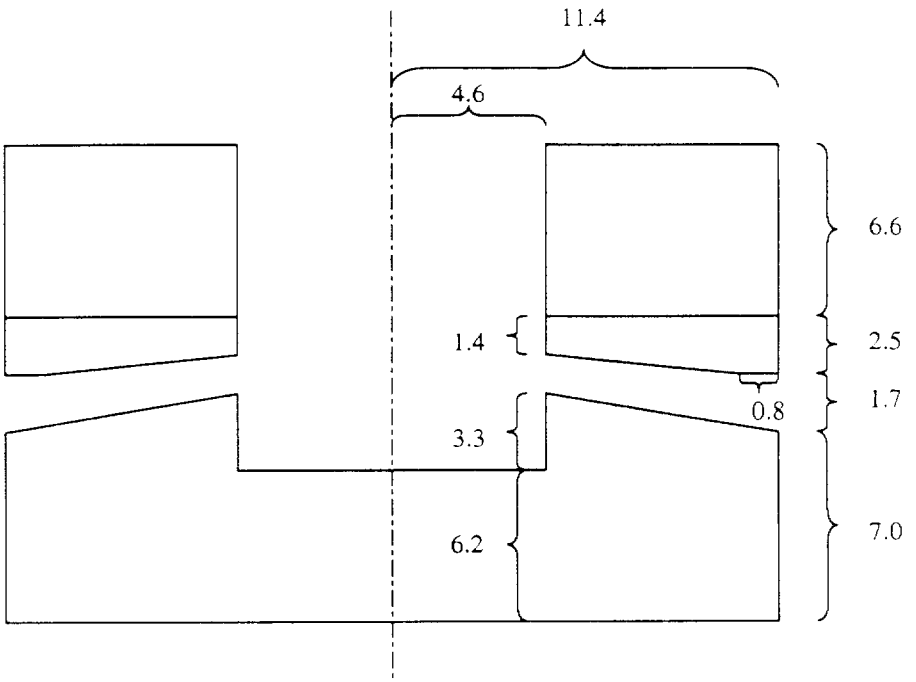
11.4
4.6
6.6
1.4
2.5
0.8
1.7
3.3
6.2
7.0

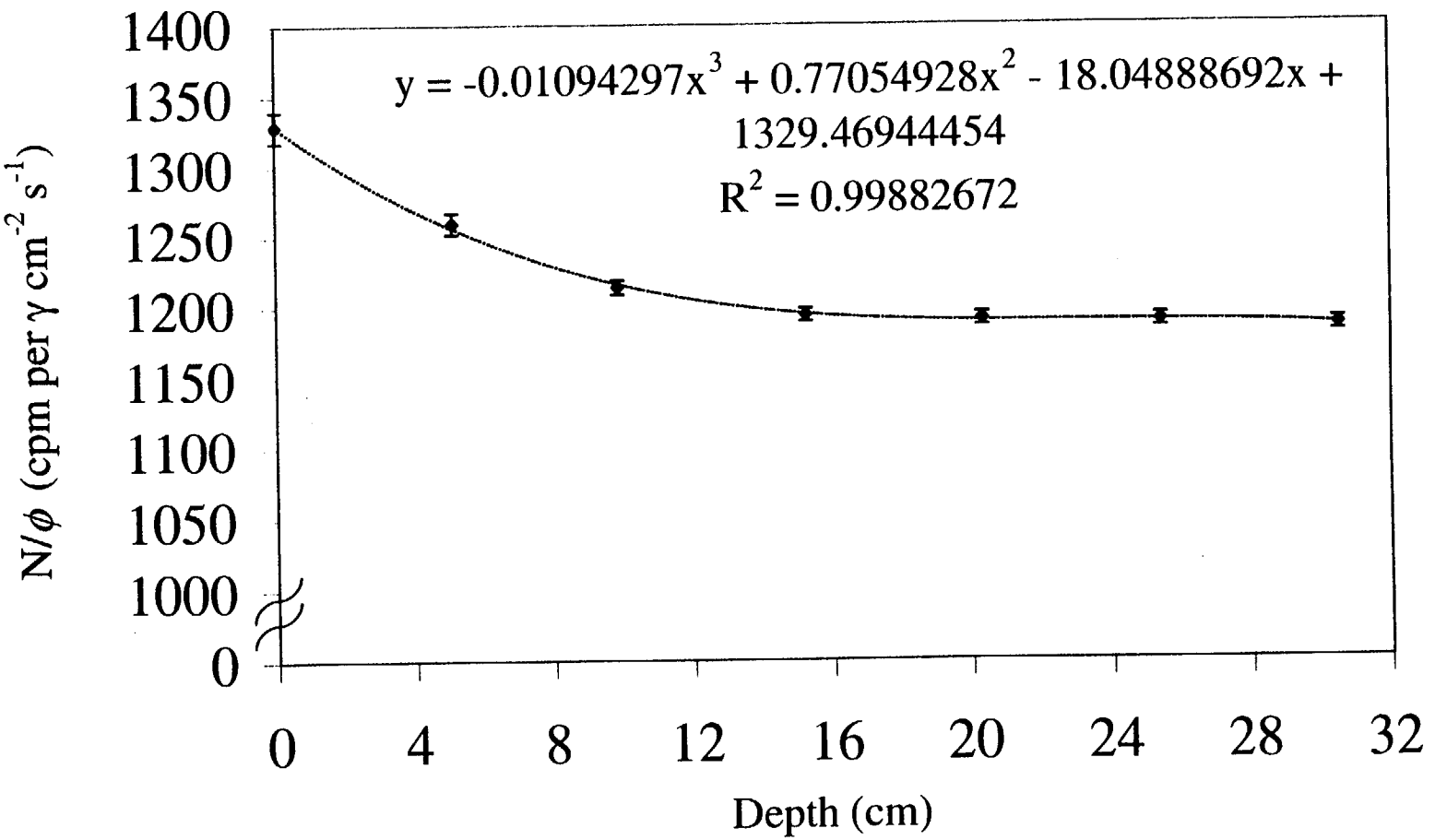
y = -0.01094297x^3 + 0.77054928x^2 - 18.04888692x + 1329.46944454
R^2 = 0.99882672
1400
1350
1300
1250
1200
1150
1100
1050
1000
0
N/φ (cpm per γ cm^-2 s^-1)
0
4
8
12
16
20
24
28
32
Depth (cm)

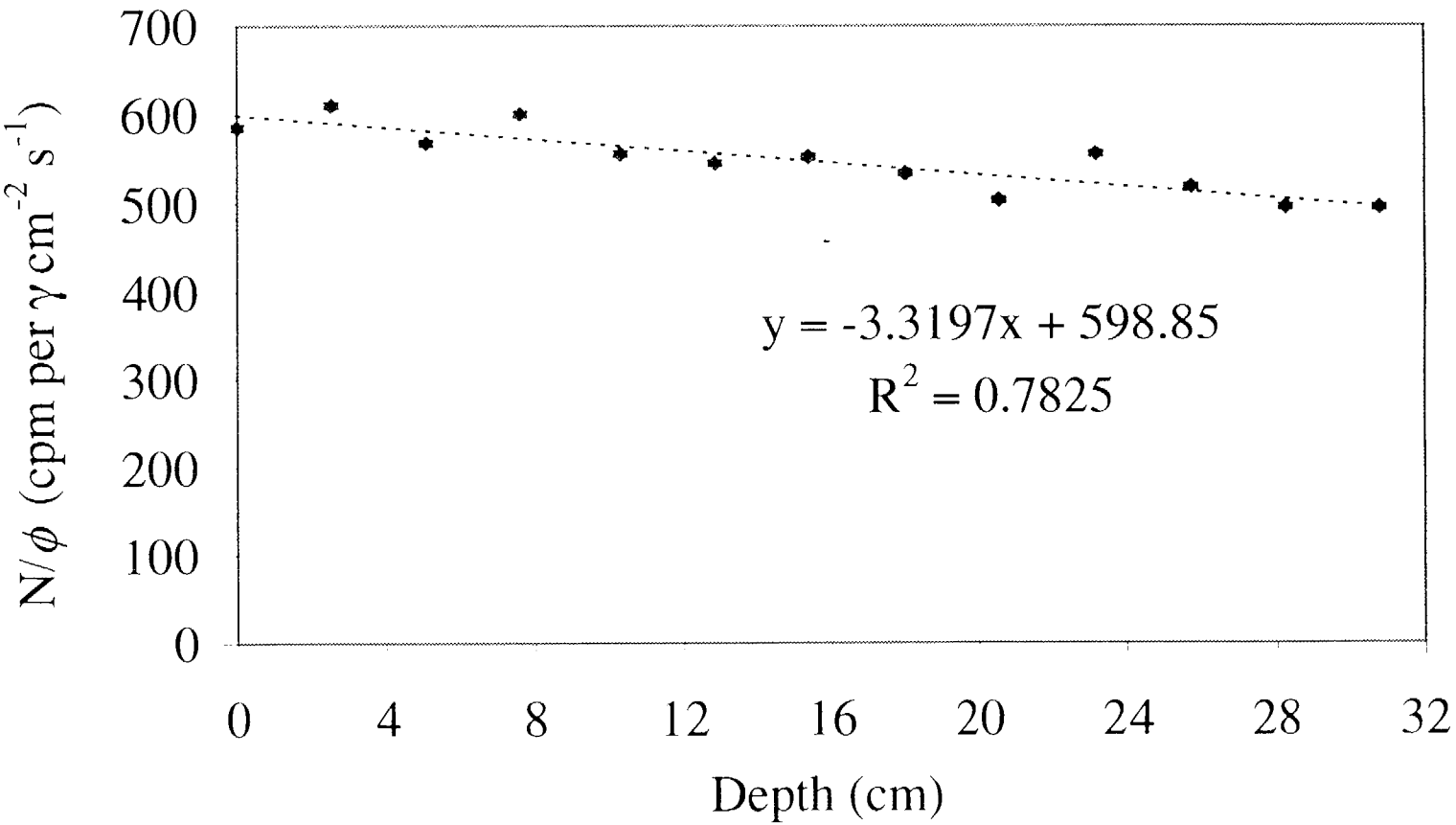
700
600
500
400
300
200
100
0
N/ϕ (cpm per γ cm-2 s-1)
y = -3.3197x + 598.85
R2 = 0.7825
0
4
8
12
16
20
24
28
32
Depth (cm)

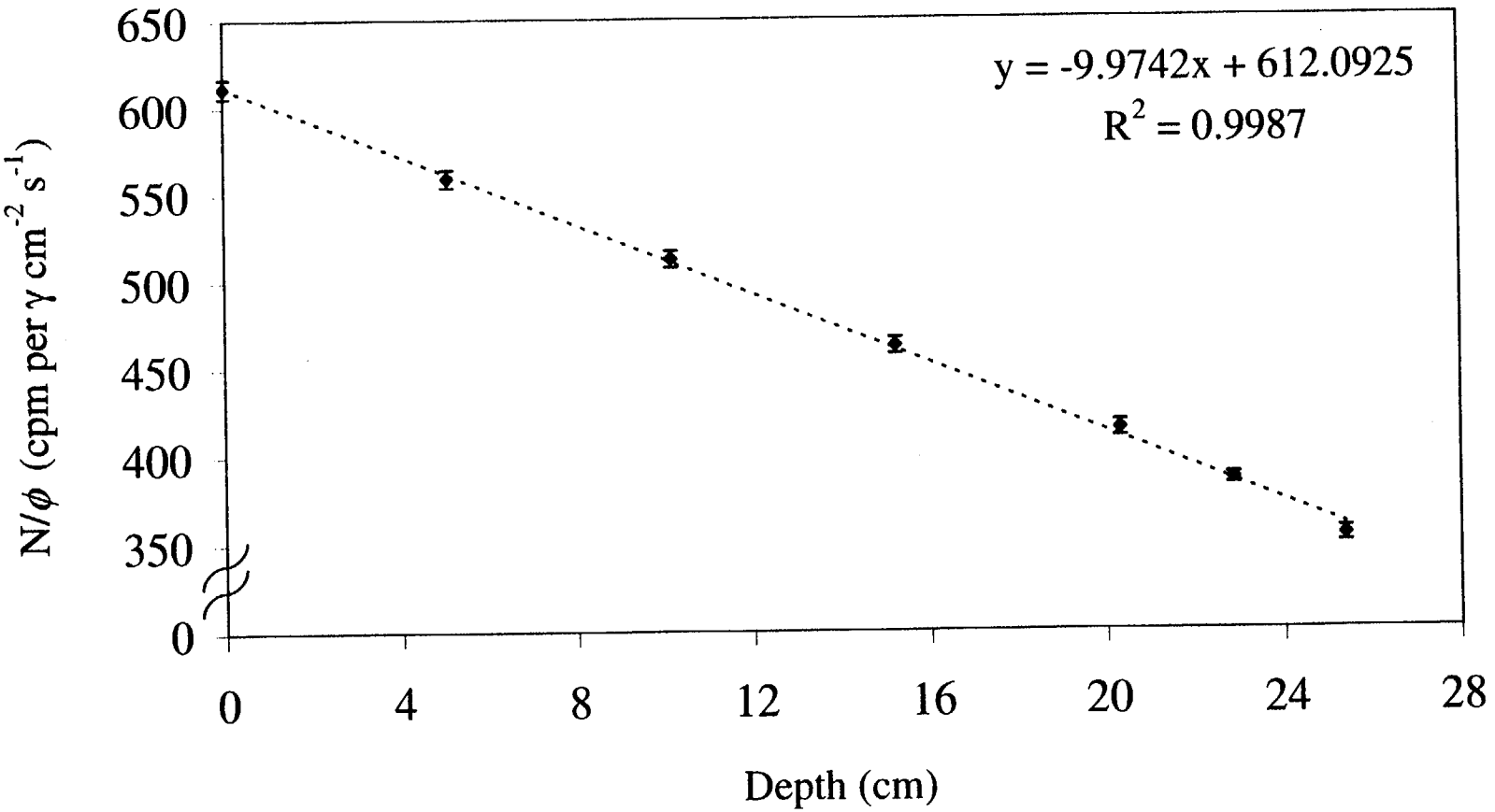
650
600
550
500
450
400
350
0
0
4
8
12
16
20
24
28
y = -9.9742x + 612.0925
R2 = 0.9987
N/ϕ (cpm per γ cm-2 s-1)
Depth (cm)

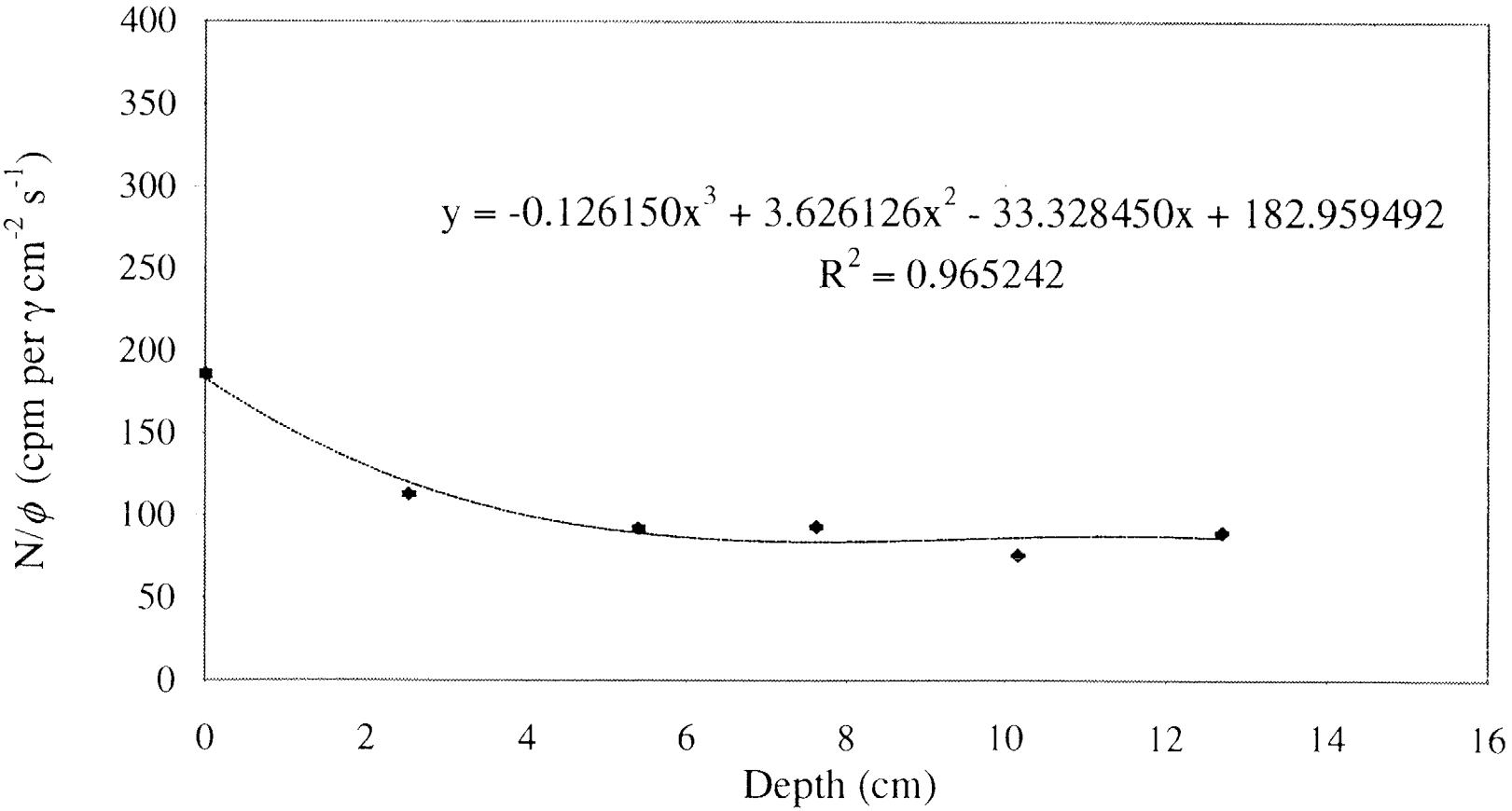
400
350
300
250
200
150
100
50
0
N/ϕ (cpm per γ cm-2 s-1)
y = -0.126150x3 + 3.626126x2 - 33.328450x + 182.959492
R2 = 0.965242
0
2
4
6
8
10
12
14
16
Depth (cm)

(a)

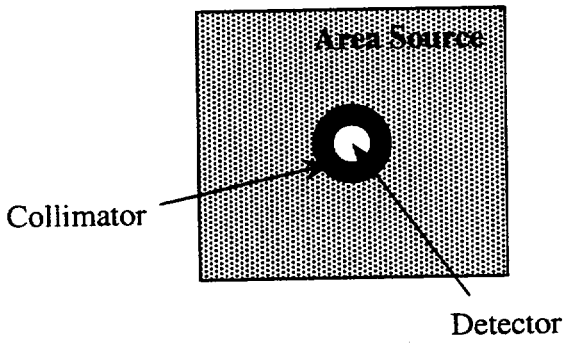
Area Source
Collimator
Detector

(b)

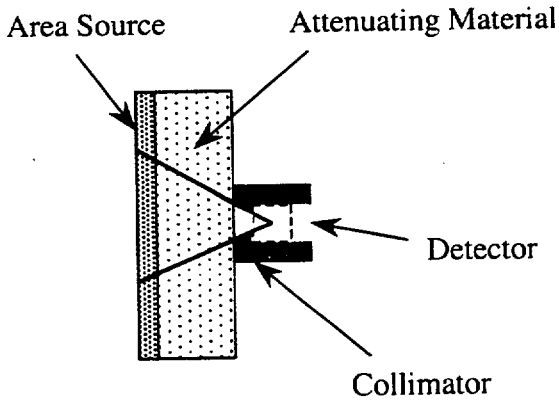
Area Source
Attenuating Material
Detector
Collimator

(a)

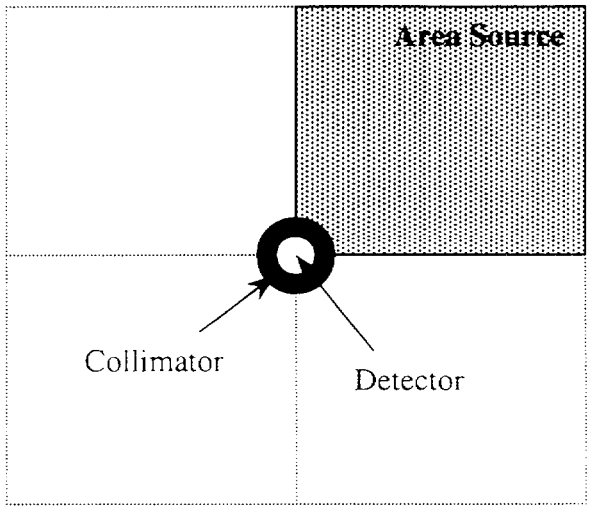
Area Source
Collimator
Detector

(b)

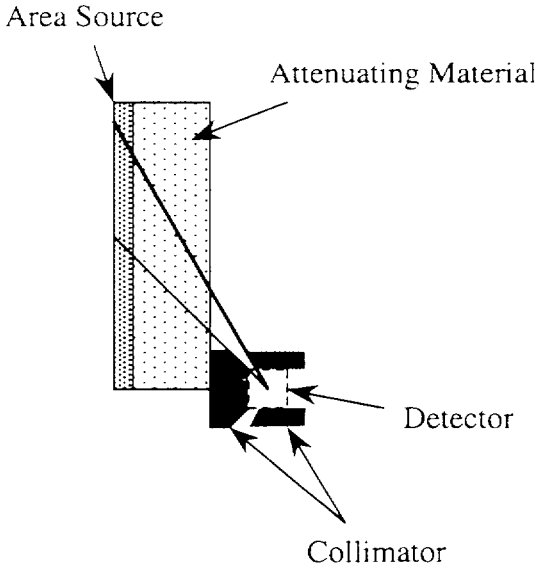
Area Source
Attenuating Material
Detector
Collimator

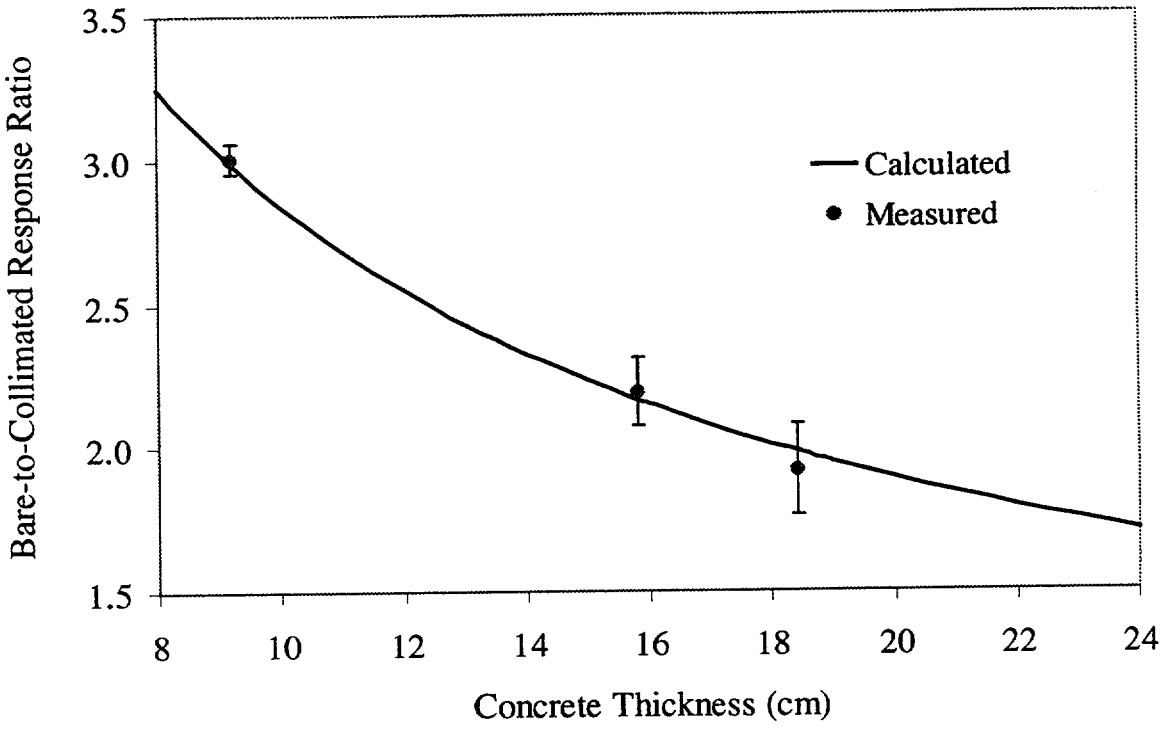
Bare-to-Collimated Response Ratio
3.5
3.0
2.5
2.0
1.5
8
10
12
14
16
18
20
22
24
Concrete Thickness (cm)
Calculated
Measured

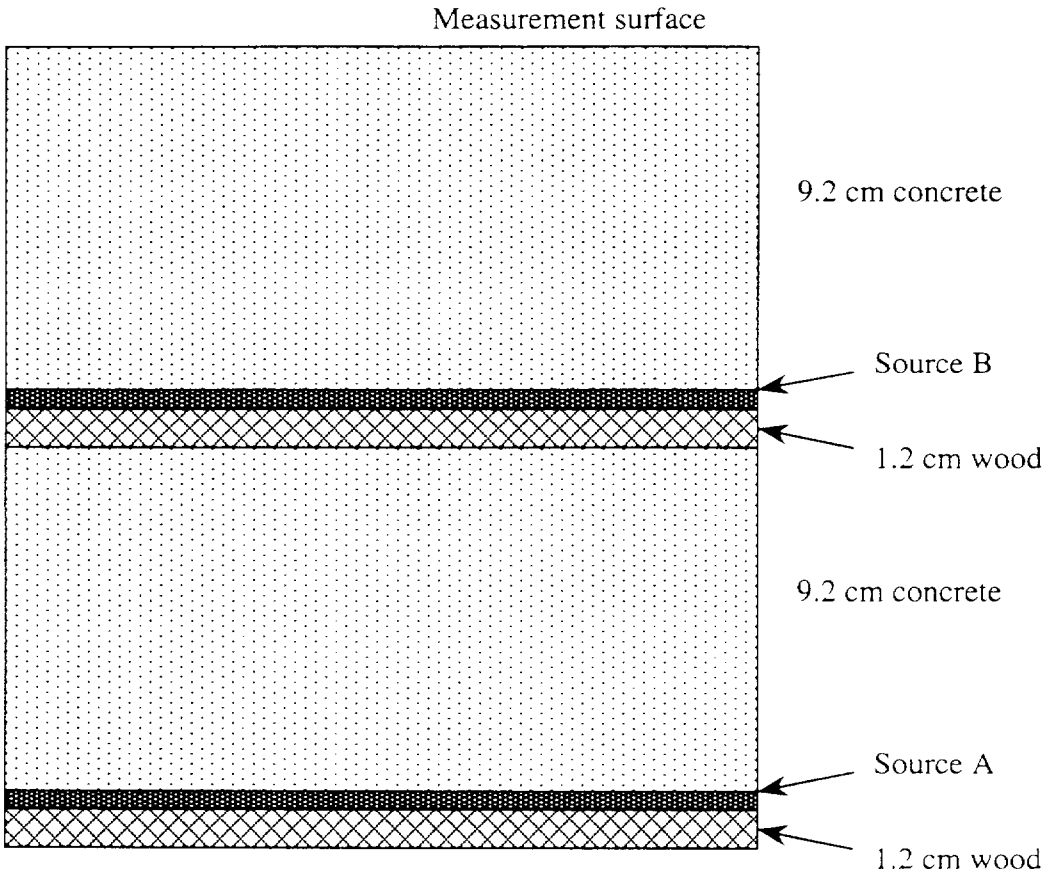
Measurement surface
9.2 cm concrete
Source B
1.2 cm wood
9.2 cm concrete
Source A
1.2 cm wood

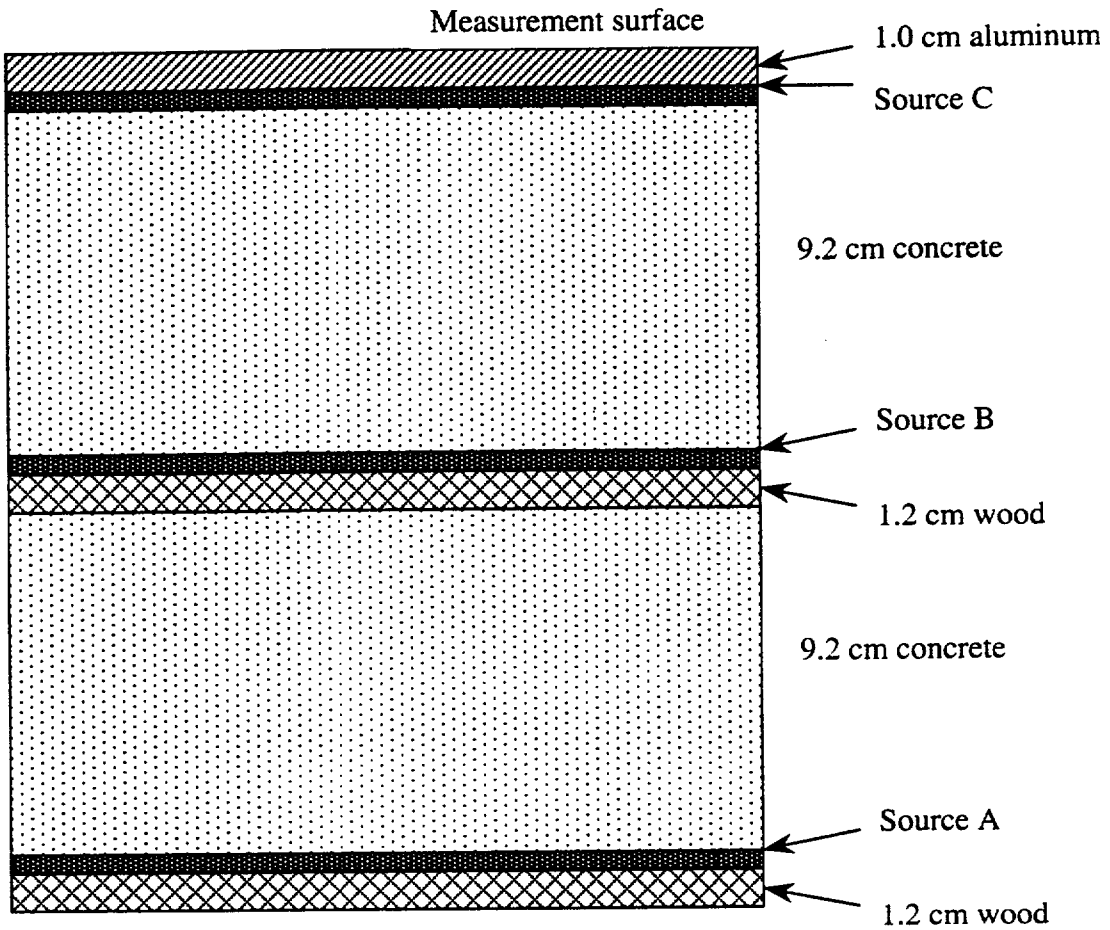
Measurement surface
1.0 cm aluminum
Source C
9.2 cm concrete
Source B
1.2 cm wood
9.2 cm concrete
Source A
1.2 cm wood

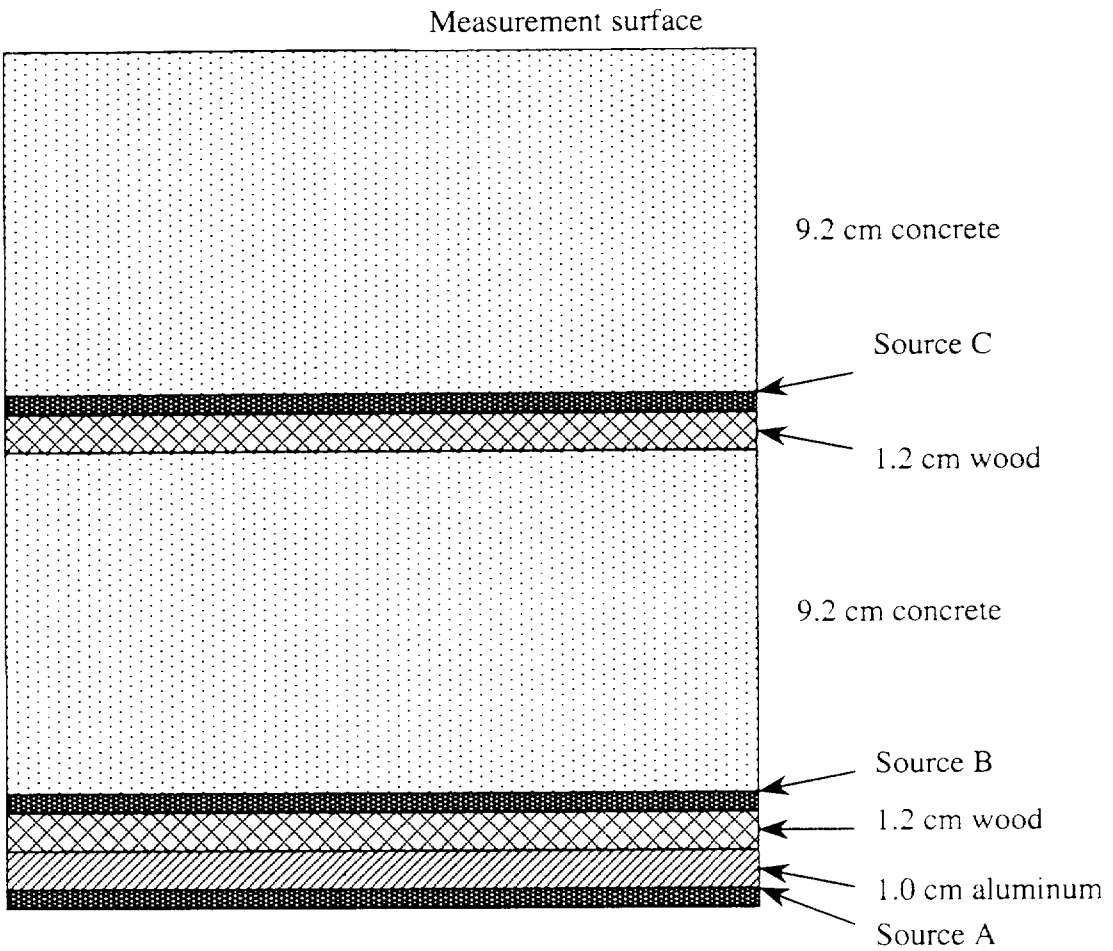
Measurement surface
9.2 cm concrete
Source C
1.2 cm wood
9.2 cm concrete
Source B
1.2 cm wood
1.0 cm aluminum
Source A

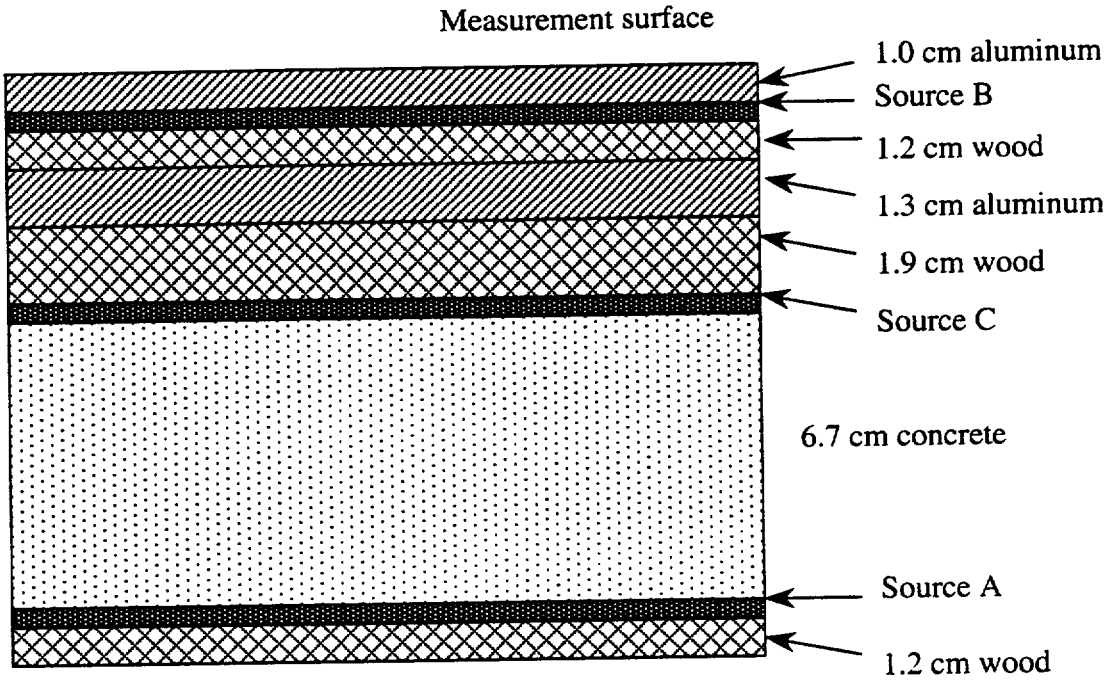
Measurement surface
1.0 cm aluminum
Source B
1.2 cm wood
1.3 cm aluminum
1.9 cm wood
Source C
6.7 cm concrete
Source A
1.2 cm wood

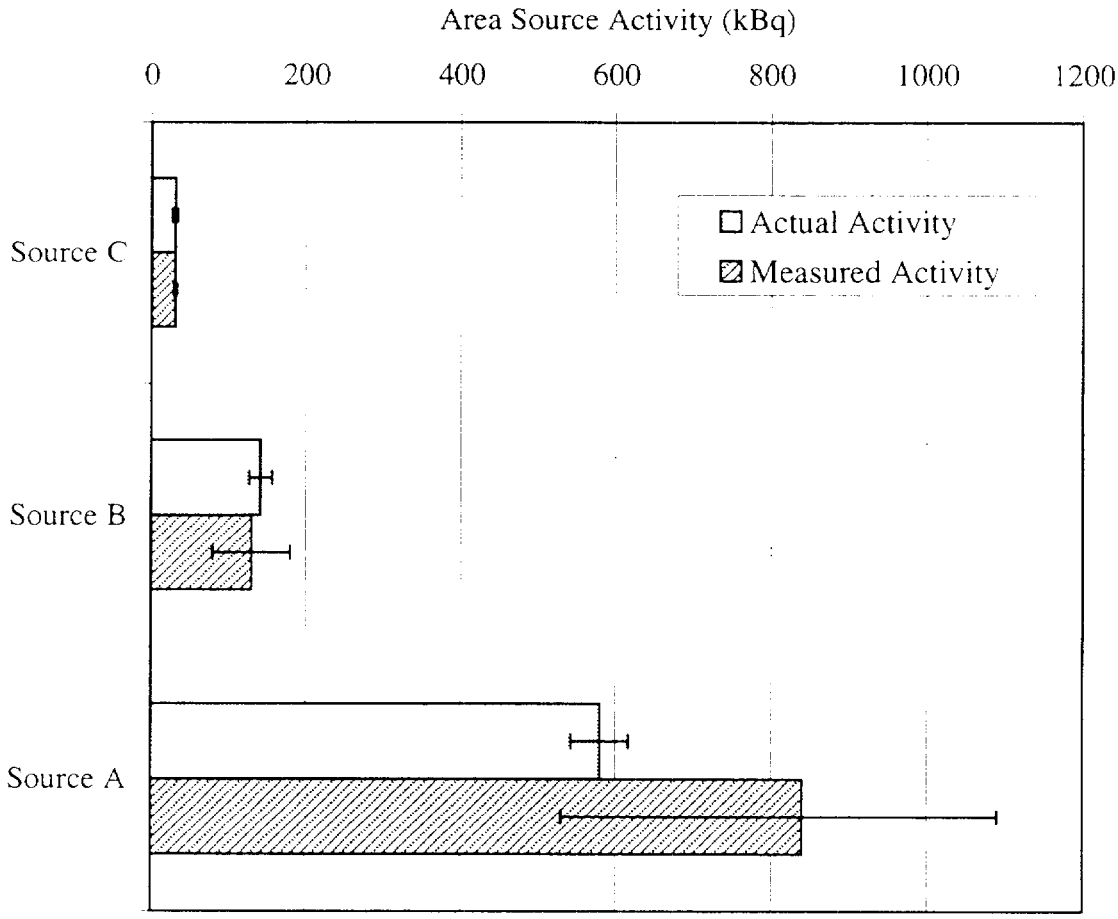
Area Source Activity (kBq)
0
200
400
600
800
1000
1200
Source C
Source B
Source A
Actual Activity
Measured Activity

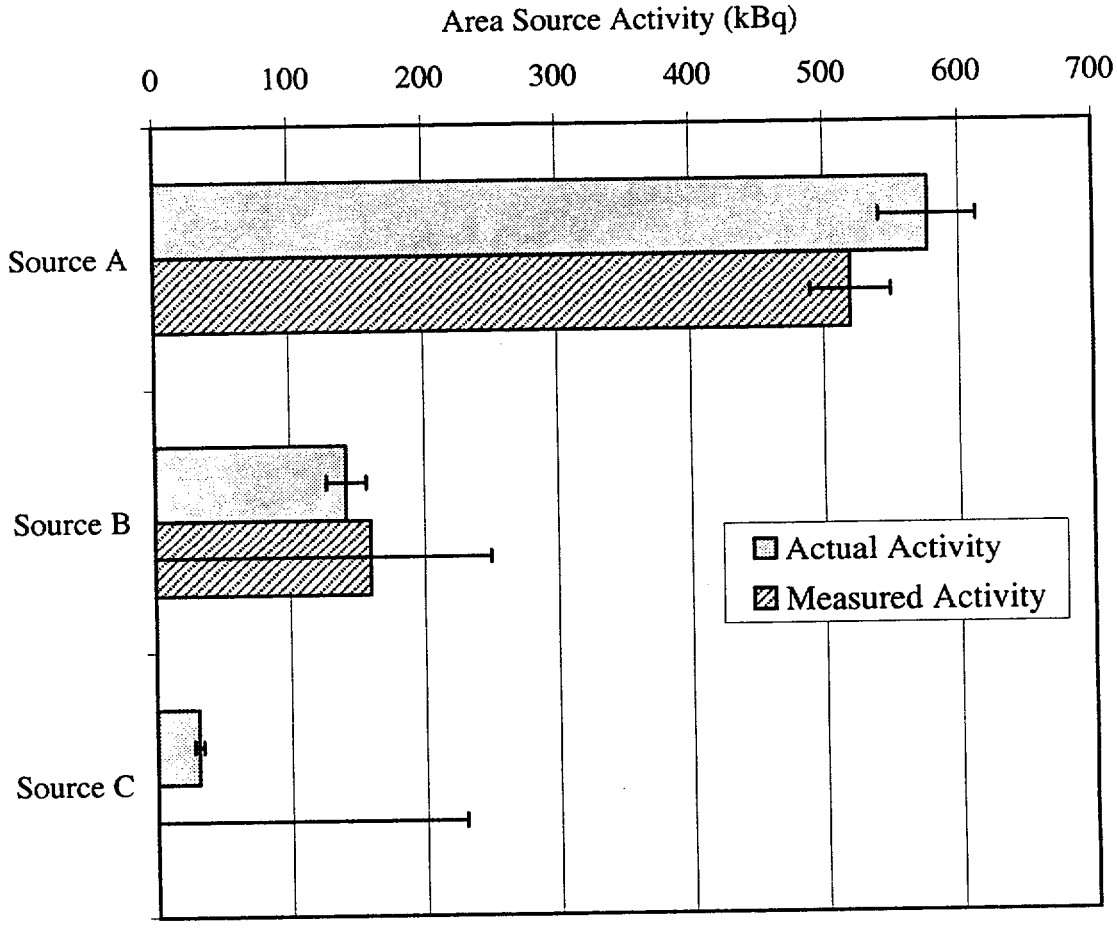
Area Source Activity (kBq)
0
100
200
300
400
500
600
700
Source A
Source B
Source C
Actual Activity
Measured Activity

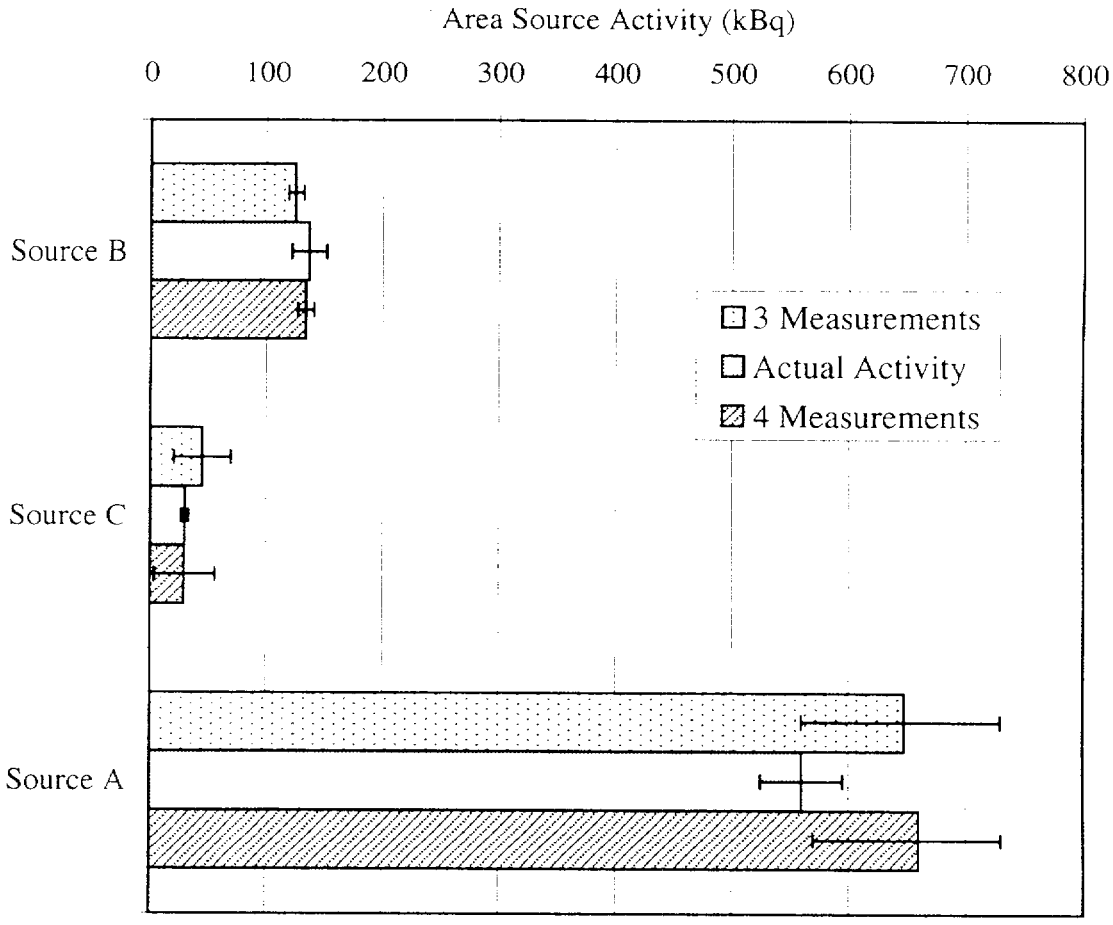
Area Source Activity (kBq)
0
100
200
300
400
500
600
700
800
Source B
Source C
Source A
3 Measurements
Actual Activity
4 Measurements

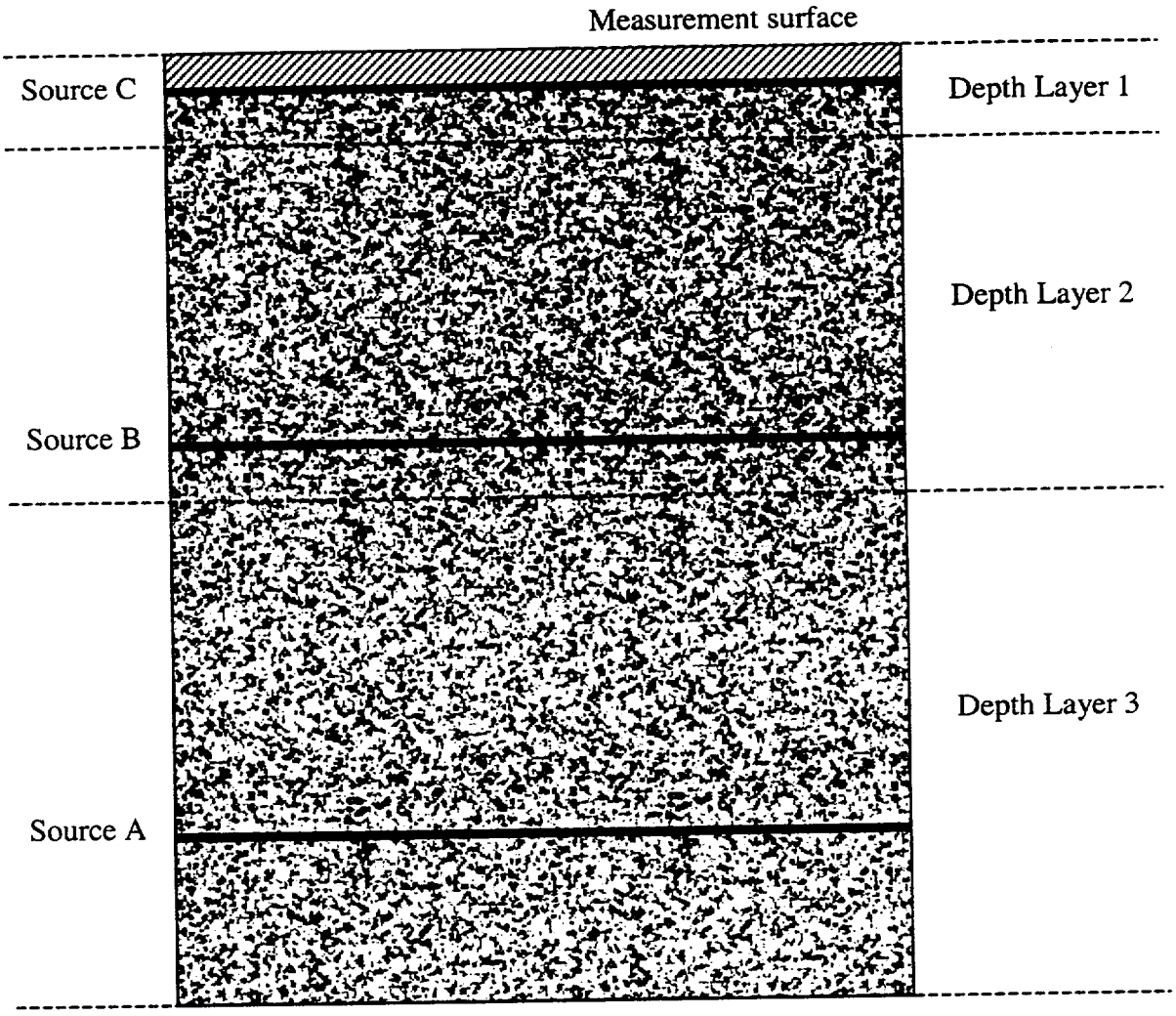
Measurement surface
Source C
Depth Layer 1
Depth Layer 2
Source B
Depth Layer 3
Source A

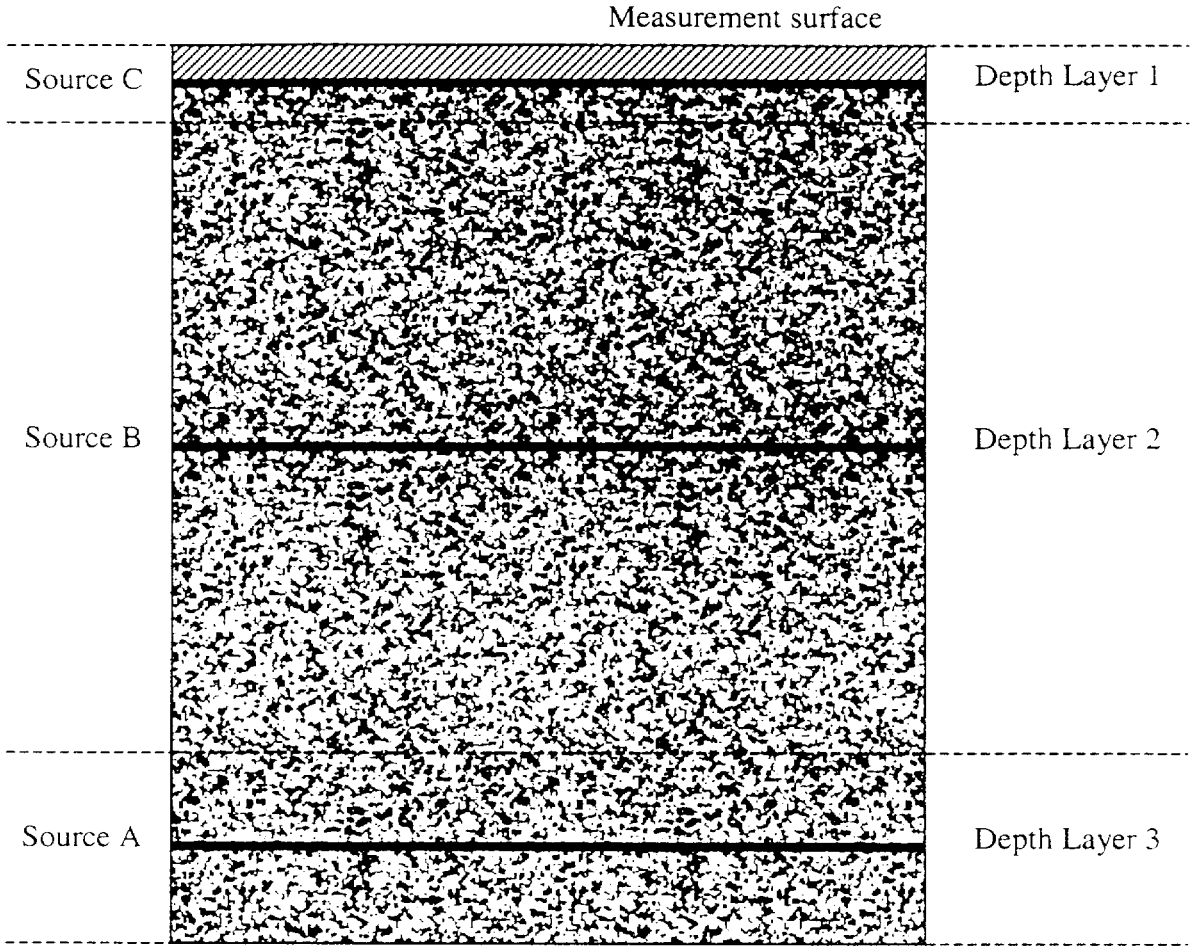
Measurement surface
Source C
Depth Layer 1
Source B
Depth Layer 2
Source A
Depth Layer 3

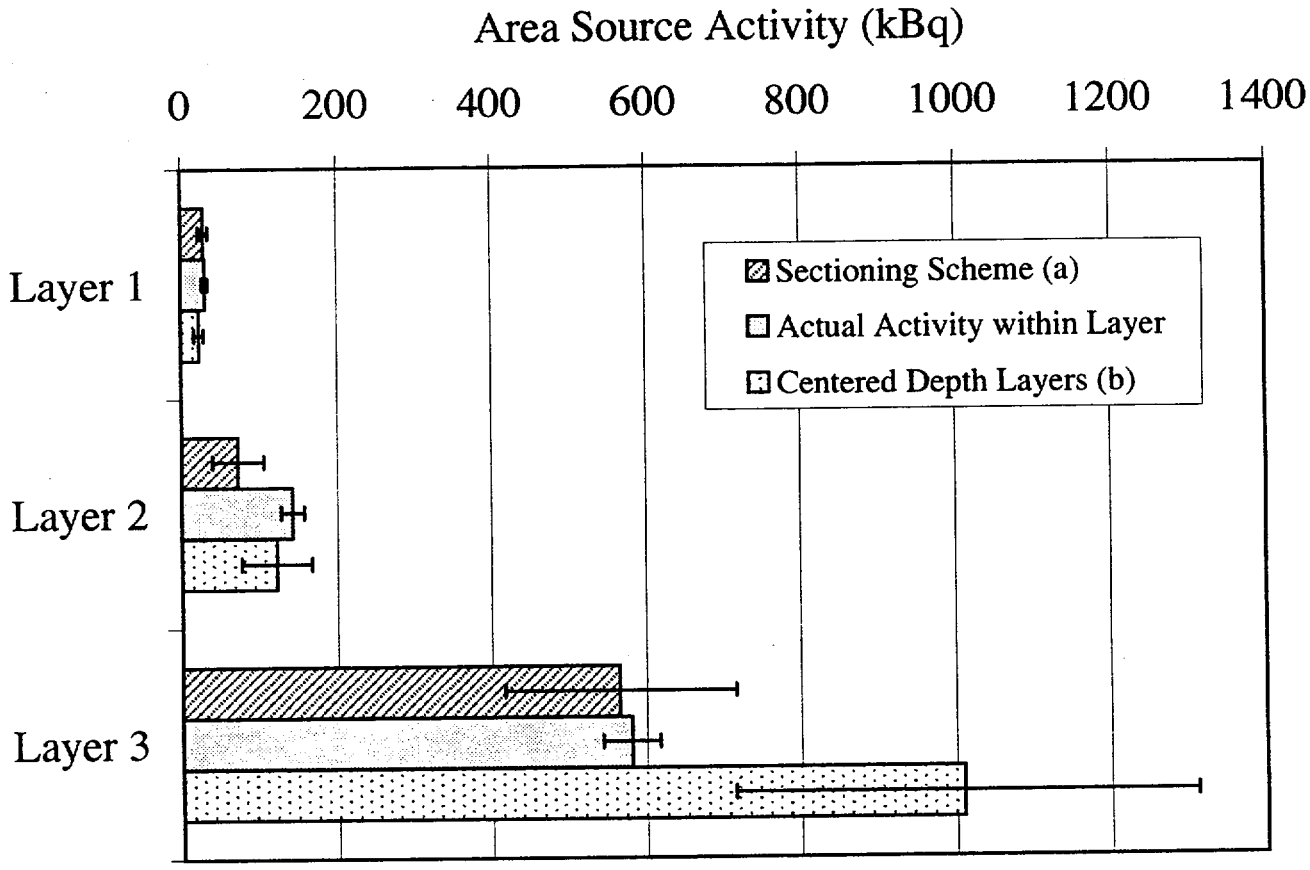
Area Source Activity (kBq)
0
200
400
600
800
1000
1200
1400
Layer 1
Layer 2
Layer 3
Sectioning Scheme (a)
Actual Activity within Layer
Centered Depth Layers (b)